



ASTRO-H Space X-ray Observatory White Paper

Older Supernova Remnants and Pulsar Wind Nebulae

K. S. Long (STScI), A. Bamba (Aoyama Gakuin University), F. Aharonian (DIAS & MPI-K),
 A. Foster (Harvard-Smithsonian Center for Astrophysics), S. Funk (Stanford University),
 J. Hiraga (University of Tokyo), J. Hughes (Rutgers University), M. Ishida (JAXA), S. Katsuda (JAXA),
 H. Matsumoto (Nagoya University), K. Mori (Miyazaki University), H. Nakajima (Osaka University),
 T. Nakamori (Yamagata University), M. Ozaki (JAXA), S. Safi-Harb (University of Manitoba),
 M. Sawada (Aoyama Gakuin University), T. Tamagawa (RIKEN), K. Tamura (Nagoya University),
 T. Tanaka (Kyoto University), H. Tsunemi (Osaka University), H. Uchida (Kyoto University),
 Y. Uchiyama (Rikkyo University), and S. Yamauchi (Nara Womens University)
 on behalf of the ASTRO-H Science Working Group

Abstract

Most supernova remnants (SNRs) are old, in the sense that their structure has been profoundly modified by their interaction with the surrounding interstellar medium (ISM). Old SNRs are very heterogeneous in terms of their appearance, reflecting differences in their evolutionary state, the environments in which SNe explode and in the explosion products. Some old SNRs are seen primarily as a result of a strong shock wave interacting with the ISM. Others, the so-called mixed-morphology SNRs, show central concentrations of emission, which may still show evidence of emission from the ejecta. Yet others, the pulsar wind nebulae (PWNe), are seen primarily as a result of emission powered by a pulsar; these SNRs often lack the detectable thermal emission from the primary shock. The underlying goal in all studies of old SNRs is to understand these differences, in terms of the SNe that created them, the nature of the ISM into which they are expanding, and the fundamental physical processes that govern their evolution. Here we identify three areas of study where *ASTRO-H* can make important contributions. These are constraining abundances and physical processes in mature limb-brightened SNRs, understanding the puzzling nature of mixed-morphology SNRs, and exploring the nature of PWNe. The Soft X-ray Spectrometer (SXS) on-board *ASTRO-H* will, as a result of its high spectral resolution, be the primary tool for addressing problems associated with old SNRs, supported by hard X-ray observations with the Hard X-ray Imager (HXI) to obtain broad band X-ray coverage.

Complete list of the ASTRO-H Science Working Group

Tadayuki Takahashi^a, Kazuhisa Mitsuda^a, Richard Kelley^b, Felix Aharonian^c, Hiroki Akamatsu^d, Fumie Akimoto^e, Steve Allen^f, Naohisa Anabuki^g, Lorella Angelini^b, Keith Arnaud^b, Marc Audardⁱ, Hisamitsu Awaki^j, Aya Bamba^k, Marshall Bautz^l, Roger Blandford^f, Laura Brenneman^b, Greg Brown^m, Edward Cackettⁿ, Maria Chernyakova^c, Meng Chiao^b, Paolo Coppi^o, Elisa Costantini^d, Jelle de Plaa^d, Jan-Willem den Herder^d, Chris Done^p, Tadayasu Dotani^a, Ken Ebisawa^a, Megan Eckart^b, Teruaki Enoto^q, Yuichiro Ezoe^r, Andrew Fabianⁿ, Carlo Ferrignoⁱ, Adam Foster^s, Ryuichi Fujimoto^t, Yasushi Fukazawa^u, Stefan Funk^f, Akihiro Furuzawa^e, Massimiliano Galeazzi^v, Luigi Gallo^w, Poshak Gandhi^p, Matteo Guainazzi^x, Yoshito Haba^y, Kenji Hamaguchi^h, Isamu Hatsukade^z, Takayuki Hayashi^a, Katsuhiro Hayashi^a, Kiyoshi Hayashida^g, Junko Hiraga^{aa}, Ann Hornschemeier^b, Akio Hoshino^{ab}, John Hughes^{ac}, Una Hwang^{ad}, Ryo Iizuka^a, Yoshiyuki Inoue^a, Hajime Inoue^a, Kazunori Ishibashi^e, Manabu Ishida^a, Kumi Ishikawa^q, Yoshitaka Ishisaki^f, Masayuki Ito^{ae}, Naoko Iyomoto^{af}, Jelle Kaastra^d, Timothy Kallman^b, Tuneyoshi Kamae^f, Jun Kataoka^{ag}, Satoru Katsuda^a, Junichiro Katsuta^u, Madoka Kawaharada^a, Nobuyuki Kawai^{ah}, Dmitry Khangulyan^a, Caroline Kilbourne^b, Masashi Kimura^{ai}, Shunji Kitamoto^{ab}, Tetsu Kitayama^{aj}, Takayoshi Kohmura^{ak}, Motohide Kokubun^a, Saori Konami^r, Katsuji Koyama^{al}, Hans Krimm^b, Aya Kubota^{am}, Hideyo Kunieda^e, Stephanie LaMassa^o, Philippe Laurent^{an}, François Lebrun^{an}, Maurice Leutenegger^b, Olivier Limousin^{an}, Michael Loewenstein^b, Knox Long^{ao}, David Lumb^{ap}, Grzegorz Madejski^f, Yoshitomo Maeda^a, Kazuo Makishima^{aa}, Maxim Markevitch^b, Hironori Matsumoto^e, Kyoko Matsushita^{aq}, Dan McCammon^{af}, Brian McNamara^{as}, Jon Miller^{at}, Eric Miller^l, Shin Mineshige^{au}, Ikuyuki Mitsuishi^e, Takuya Miyazawa^e, Tsunefumi Mizuno^u, Koji Mori^z, Hideyuki Mori^e, Koji Mukai^b, Hiroshi Murakami^{av}, Toshio Murakami^t, Richard Mushotzky^h, Ryo Nagino^g, Takao Nakagawa^a, Hiroshi Nakajima^g, Takeshi Nakamori^{aw}, Shinya Nakashima^a, Kazuhiro Nakazawa^{aa}, Masayoshi Nobukawa^{al}, Hirofumi Noda^q, Masaharu Nomachi^{ax}, Steve O' Dell^{ay}, Hirokazu Odaka^a, Takaya Ohashi^r, Masanori Ohno^u, Takashi Okajima^b, Naomi Ota^{az}, Masanobu Ozaki^a, Frits Paerels^{ba}, Stéphane Paltaniⁱ, Arvind Parmar^x, Robert Petre^b, Ciro Pintoⁿ, Martin Pohlⁱ, F. Scott Porter^b, Katja Pottschmidt^b, Brian Ramsey^{ay}, Rubens Reis^{at}, Christopher Reynolds^h, Claudio Ricci^{au}, Helen Russellⁿ, Samar Safi-Harb^{bb}, Shinya Saito^a, Hiroaki Sameshima^a, Goro Sato^{ag}, Kosuke Sato^{aq}, Rie Sato^a, Makoto Sawada^k, Peter Serlemitsos^b, Hiromi Seta^{bc}, Aurora Simionescu^a, Randall Smith^s, Yang Soong^b, Łukasz Stawarz^a, Yasuharu Sugawara^{bd}, Satoshi Sugita^j, Andrew Szymkowiak^o, Hiroyasu Tajima^e, Hiromitsu Takahashi^u, Hiroaki Takahashi^g, Yoh Takei^a, Toru Tamagawa^q, Takayuki Tamura^a, Keisuke Tamura^e, Takaaki Tanaka^{al}, Yasuo Tanaka^a, Yasuyuki Tanaka^u, Makoto Tashiro^{bc}, Yuzuru Tawara^e, Yukikatsu Terada^{bc}, Yuichi Terashima^j, Francesco Tombesi^b, Hiroshi Tomida^{ai}, Yohko Tsuboi^{bd}, Masahiro Tsujimoto^a, Hiroshi Tsunemi^g, Takeshi Tsuru^{al}, Hiroyuki Uchida^{al}, Yasunobu Uchiyama^{ab}, Hideki Uchiyama^{be}, Yoshihiro Ueda^{au}, Shutaro Ueda^g, Shiro Ueno^{ai}, Shinichiro Uno^{bf}, Meg Urry^o, Eugenio Ursino^v, Cor de Vries^d, Shin Watanabe^a, Norbert Werner^f, Dan Wilkins^w, Shinya Yamada^r, Hiroya Yamaguchi^b, Kazutaka Yamaoka^e, Noriko Yamasaki^a, Makoto Yamauchi^z, Shigeo Yamauchi^{az}, Tahir Yaqoob^b, Yoichi Yatsu^{ah}, Daisuke Yonetoku^t, Atsumasa Yoshida^k, Takayuki Yuasa^q, Irina Zhuravleva^f, Abderahmen Zoghbi^h, and John ZuHone^b

^aInstitute of Space and Astronautical Science (ISAS), Japan Aerospace Exploration Agency (JAXA), Kanagawa 252-5210, Japan

^bNASA/Goddard Space Flight Center, MD 20771, USA

^cAstronomy and Astrophysics Section, Dublin Institute for Advanced Studies, Dublin 2, Ireland

^dSRON Netherlands Institute for Space Research, Utrecht, The Netherlands

^eDepartment of Physics, Nagoya University, Aichi 338-8570, Japan

^fKavli Institute for Particle Astrophysics and Cosmology, Stanford University, CA 94305, USA

^gDepartment of Earth and Space Science, Osaka University, Osaka 560-0043, Japan

^hDepartment of Astronomy, University of Maryland, MD 20742, USA

ⁱUniversité de Genève, Genève 4, Switzerland

^jDepartment of Physics, Ehime University, Ehime 790-8577, Japan

^kDepartment of Physics and Mathematics, Aoyama Gakuin University, Kanagawa 229-8558, Japan

^lKavli Institute for Astrophysics and Space Research, Massachusetts Institute of Technology, MA 02139, USA

^mLawrence Livermore National Laboratory, CA 94550, USA

ⁿInstitute of Astronomy, Cambridge University, CB3 0HA, UK

^oYale Center for Astronomy and Astrophysics, Yale University, CT 06520-8121, USA

^pDepartment of Physics, University of Durham, DH1 3LE, UK

^qRIKEN, Saitama 351-0198, Japan

^rDepartment of Physics, Tokyo Metropolitan University, Tokyo 192-0397, Japan

^sHarvard-Smithsonian Center for Astrophysics, MA 02138, USA

- ¹Faculty of Mathematics and Physics, Kanazawa University, Ishikawa 920-1192, Japan
- ^uDepartment of Physical Science, Hiroshima University, Hiroshima 739-8526, Japan
- ^vPhysics Department, University of Miami, FL 33124, USA
- ^wDepartment of Astronomy and Physics, Saint Mary's University, Nova Scotia B3H 3C3, Canada
- ^xEuropean Space Agency (ESA), European Space Astronomy Centre (ESAC), Madrid, Spain
- ^yDepartment of Physics and Astronomy, Aichi University of Education, Aichi 448-8543, Japan
- ^zDepartment of Applied Physics, University of Miyazaki, Miyazaki 889-2192, Japan
- ^{aa}Department of Physics, University of Tokyo, Tokyo 113-0033, Japan
- ^{ab}Department of Physics, Rikkyo University, Tokyo 171-8501, Japan
- ^{ac}Department of Physics and Astronomy, Rutgers University, NJ 08854-8019, USA
- ^{ad}Department of Physics and Astronomy, Johns Hopkins University, MD 21218, USA
- ^{ae}Faculty of Human Development, Kobe University, Hyogo 657-8501, Japan
- ^{af}Kyushu University, Fukuoka 819-0395, Japan
- ^{ag}Research Institute for Science and Engineering, Waseda University, Tokyo 169-8555, Japan
- ^{ah}Department of Physics, Tokyo Institute of Technology, Tokyo 152-8551, Japan
- ^{ai}Tsukuba Space Center (TKSC), Japan Aerospace Exploration Agency (JAXA), Ibaraki 305-8505, Japan
- ^{aj}Department of Physics, Toho University, Chiba 274-8510, Japan
- ^{ak}Department of Physics, Tokyo University of Science, Chiba 278-8510, Japan
- ^{al}Department of Physics, Kyoto University, Kyoto 606-8502, Japan
- ^{am}Department of Electronic Information Systems, Shibaura Institute of Technology, Saitama 337-8570, Japan
- ^{an}IRFU/Service d'Astrophysique, CEA Saclay, 91191 Gif-sur-Yvette Cedex, France
- ^{ao}Space Telescope Science Institute, MD 21218, USA
- ^{ap}European Space Agency (ESA), European Space Research and Technology Centre (ESTEC), 2200 AG Noordwijk, The Netherlands
- ^{aq}Department of Physics, Tokyo University of Science, Tokyo 162-8601, Japan
- ^{ar}Department of Physics, University of Wisconsin, WI 53706, USA
- ^{as}University of Waterloo, Ontario N2L 3G1, Canada
- ^{at}Department of Astronomy, University of Michigan, MI 48109, USA
- ^{au}Department of Astronomy, Kyoto University, Kyoto 606-8502, Japan
- ^{av}Department of Information Science, Faculty of Liberal Arts, Tohoku Gakuin University, Miyagi 981-3193, Japan
- ^{aw}Department of Physics, Faculty of Science, Yamagata University, Yamagata 990-8560, Japan
- ^{ax}Laboratory of Nuclear Studies, Osaka University, Osaka 560-0043, Japan
- ^{ay}NASA/Marshall Space Flight Center, AL 35812, USA
- ^{az}Department of Physics, Faculty of Science, Nara Women's University, Nara 630-8506, Japan
- ^{ba}Department of Astronomy, Columbia University, NY 10027, USA
- ^{bb}Department of Physics and Astronomy, University of Manitoba, MB R3T 2N2, Canada
- ^{bc}Department of Physics, Saitama University, Saitama 338-8570, Japan
- ^{bd}Department of Physics, Chuo University, Tokyo 112-8551, Japan
- ^{be}Science Education, Faculty of Education, Shizuoka University, Shizuoka 422-8529, Japan
- ^{bf}Faculty of Social and Information Sciences, Nihon Fukushi University, Aichi 475-0012, Japan

Contents

1	Limb brightened SNRs and the physics of shocks	5
1.1	Background and Previous Studies	5
1.2	Prospects & Strategy	5
1.3	Targets & Feasibility	6
1.3.1	Cygnus Loop - A prototypical limb-brightened SNR	6
1.3.2	Cygnus Loop - Solving the low abundance problem	8
1.3.3	Cygnus Loop – Shock Cloud Interactions	9
1.3.4	Cygnus Loop – Nature of the progenitor	10
1.3.5	Vela SNR - Background	10
1.3.6	Using velocity-broadening to measure ejecta metallicity in the Vela SNR through observations of “shrapnel”	13
2	Mixed-Morphology Supernova Remnants	14
2.1	Background and Previous Studies	14
2.2	Prospects & Strategy	15
2.3	Targets & Feasibility	16
2.3.1	W49B	16
2.3.2	Other potential targets	17
2.4	Beyond Feasibility	18
3	Pulsar Wind Nebulae and their Evolution	18
3.1	Background and Previous Studies	18
3.2	Prospects & Strategy	20
3.3	Targets & Feasibility	20
3.4	Beyond Feasibility	22
4	Conclusions for Old SNRs and Pulsar Wind Nebulae	23

Supernova remnants (SNRs) represent a crucial phase in the life cycle of stars and galaxies, a phase during which the energy of a SN explosion is transferred to the interstellar medium (ISM) and the material generated in stars is returned to the ISM to create the next generation of stars. They also represent laboratories for understanding the physics of both thermal and non-thermal plasmas with conditions that are far different from what can be produced in any earth-based laboratory.

Most SNRs are old in the sense that they have swept up much more material than that was ejected by the exploding star. As a result, most, though not necessarily all, of the observed X-rays arise from the interaction of the shock with the ISM. If the ISM were uniform, then all SNRs would evolve through a set of well-defined stages - a free expansion phase, an adiabatic phase, and a radiative phase before merging into the ISM. Similarly, if all SN explosions were identical, we would not find some SNRs with central objects and pulsar wind nebulae and others not. Instead, SNRs are very heterogeneous in appearance as a result of a complex set of factors ranging from the nature of the SN explosion to the density and uniformity of the ISM into which they are expanding. Ideally, we would like to reduce this apparent complexity into a small number of variables that are connected concretely to the SN progenitor and the environment.

Young SNRs will be addressed in a separate white paper (Hughes et al.). Here we focus on the older SNRs, which are dominated by shocked ISM material, and on Pulsar Wind Nebulae (PWNe), the synchrotron bubbles inflated by rapidly rotating neutron stars born in core-collapse explosions. Studies of these objects shed light on basic astrophysical questions related to shock and plasma physics, the evolution of SNRs and interaction with the ISM, and the way neutron stars deposit energy into and interact with the surrounding medium.

Old SNRs can be divided into 3 subgroups: (1) Limb-brightened SNRs in which most of the observed X-ray emission arises just behind the primary shock front as it moves into the ISM, (2) Mixed-morphology SNRs in which most of the emission arises from a thermal plasma in the interior of the SNR, and (3) Pulsar Wind Nebulae, in which most of the emission arises from radiation from energetic electrons produced by an active pulsar.

1 Limb brightened SNRs and the physics of shocks

1.1 Background and Previous Studies

When a SN explodes, a strong shock is sent out into the ISM. This shock heats the material it encounters to temperatures which depend on the speed of the shock and the fraction of the shock energy that is thermalized at the shock front. In older SNRs, shock speeds are typically $100 - 500 \text{ km s}^{-1}$ and as a result, the plasma behind the shock typically has a temperature in the range 10^6 to 10^7 K. The X-ray radiation from this thermal plasma is dominated by emission lines. Studies of these emission lines provide crucial information about plasma conditions behind the shock, the abundance patterns in the post-shock gas, and atomic processes that are important in shocked plasmas.

The first imaging surveys of old SNRs were carried out using *Einstein* and *ROSAT*. The data were typically analyzed in terms of 1-dimensional Sedov models in order to infer basic properties of the SNRs, such as their approximate age and evolutionary state and the density of the ISM into which they were expanding. With the advent of CCDs, it became possible to observe individual emission lines in these SNRs, particularly at energies greater than 1 keV.

1.2 Prospects & Strategy

The rims of old SNRs are ideal sites to study dynamics of the cloud-shock interactions and of the atomic processes associated with relatively slow shocks, because line broadening is free from not only thermal Doppler broadening but also the bulk motions of the expanding shock. For shocks associated with old SNRs (the velocities are typically $100 - 500 \text{ km s}^{-1}$), it is observationally known that electrons and ions are equilibrated immediately behind the shock, making the ion temperature 1 keV or lower. Thus, expected thermal Doppler broadening is $\lesssim 0.1 \text{ eV}$, even though the shock is collisionless (e.g., Ghavamian et al., 2007). Also, the bulk

motion due to shell expansion is not of concern in the rim regions of largely extended SNRs. Thus, old SNRs provide clean laboratories for the study of plasma dynamics due to cloud-shock interactions.

There are a number of problems associated with old SNRs with limb-brightened morphologies that can be addressed with *ASTRO-H*:

First, CCD measurements of the post-shock gas of the rims of old SNRs yield metal abundances significantly lower than average Galactic ISM values. This is the case for the Cygnus Loop (e.g., Miyata et al., 1994; Katsuda et al., 2008; Uchida et al., 2009, and references therein), Puppis A (Hwang et al., 2008), RCW86 (Vink et al., 1997; Yamaguchi et al., 2008) and the Vela SNR (Miceli et al., 2008). Why this should be so is unclear. One possibility is that the shocks at the rim of old SNRs are moving into material polluted by mass loss from the pre-SN star; another is that metals are bound up in dust grains. Yet a third possibility is that atomic processes such as charge-exchange (CX) emission (Katsuda et al., 2011) and resonance line scattering (Miyata et al., 2008), which are not taken into account in the models, affect the inferred abundances. A final possibility is that inaccuracies in the models and in instrumental characteristics are introducing systematic errors in the analysis. Analysis of CCD-based data is strongly dependent both on models and on a precise understanding of instrumental parameters, because with CCD spectral resolution of ~ 100 eV, the lines used to determine abundances are often blended and not cleanly separable from the continuum, especially below 1.2 keV. Although similar problems affect observations of many other types of objects, the problem is especially severe for old SNRs, since their X-ray spectra are soft, with characteristic temperatures less than 1 keV. Many lines of N, O, Ne and Fe contribute to the spectrum between 300 eV and 1200 eV. With an energy resolution better than 7 eV, the *ASTRO-H* SXS will dramatically reduce the problems due to limited spectral resolution, and allow us to pinpoint the real cause of the low abundances reported previously.

Second, although old SNRs with limb-brightened X-ray morphologies are dominated by emission from the ISM, many, including the Cygnus Loop, Vela, RCW86 and Puppis A, show evidence of ejecta in a hotter component that is more centrally peaked than the emission from the ISM shock. Although it has been established that RCW86 is most likely the result of a Type Ia explosion, whereas the Cygnus Loop, the Vela SNR, and Puppis A are remnants of core-collapse explosions, studies of this material using the *ASTRO-H* SXS are crucial in order to determine the mass and energetics of the SN explosion that produced each of these remnants.

1.3 Targets & Feasibility

There are a large number of shell-like SNRs that could be observed with *ASTRO-H*. The two prototypical shell-like SNRs for X-ray studies are the Cygnus Loop and the Vela SNR. They have become the prototypes primarily because they are nearby and bright, which meant they were easily resolvable with the first generation imaging telescopes. They remain the best objects for studies of older SNRs for roughly the same reasons with *ASTRO-H*, and we discuss them in more detail below.

Other SNRs of interest include RCW86, which appears to be an example of a Type Ia explosion within a wind-blown bubble (Vink et al., 1997); Puppis A, which, based optical spectra and the presence of a central compact remnant, is the result of a core-collapse SN; plus a number of SNRs in the Magellanic Clouds. All have high surface brightness and therefore good spectra can be obtained with *ASTRO-H* SXS in reasonably short exposures.

1.3.1 Cygnus Loop - A prototypical limb-brightened SNR

The Cygnus Loop is one of the brightest soft X-ray sources. It is limb brightened at X-ray and radio wavelengths, and most of the observed optical emission also arises from the shell. About 3° in diameter, with a “breakout” region in the south, it lies at a distance of 540 pc (Blair et al., 2005), implying it has a diameter of about 28 pc. It is associated with the delicate optical filamentation of the Veil Nebula, which includes both Balmer-dominated and radiative shocks (see, e.g. Levenson et al., 1998). The Cygnus Loop is thought to be the result of a Type II SN explosion that took place about 10^4 years ago (even though no stellar remnant has been found). Measured shock velocities range from about 150 to 400 km s^{-1} . It is believed to be in an transition from the adiabatic to the radiative phase. The current X-ray morphology is thought to be due to the encounter

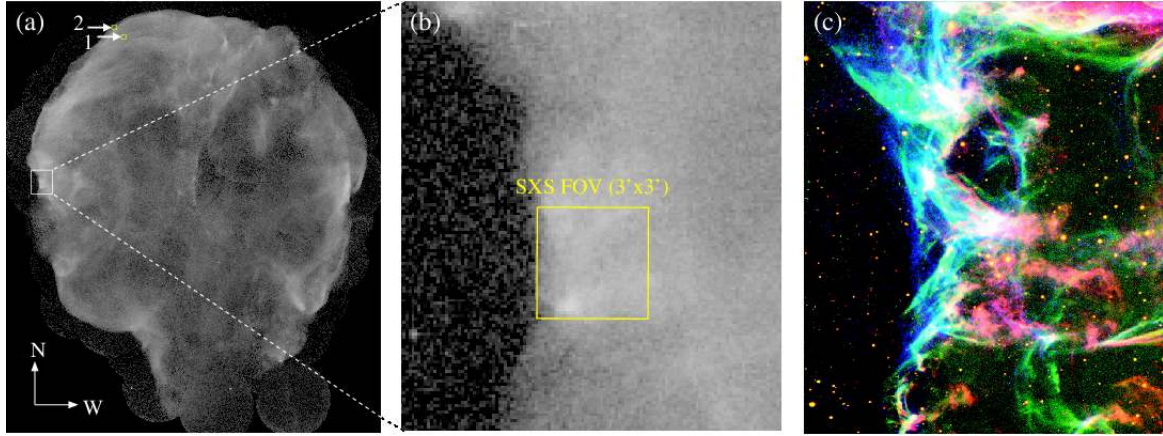


Figure 1: Left: X-ray view of the entire Cygnus Loop taken by the ROSAT HRI (Levenson et al., 1997). The so-called XA region is located within the white box. SXS simulations for the arrow-indicated yellow box regions are presented in Figure 3. Center: Close-up image of the white box region in the left panel. The SXS FOV is shown as a yellow box. Right: Optical image covering the roughly same region as in the center panel (the image is taken from Danforth et al., 2001). Red, green, and blue correspond to $H\alpha$, [O III], and the FUV, respectively.

of primary shock wave with the wall of a cavity that was generated by the pre-SN star (McCray & Snow, 1979; Levenson et al., 1998).

The Cygnus Loop has a two component thermal X-ray spectrum (Tsunemi et al., 2007). The first component, which appears to have sub-solar metal abundances and a low temperatures ($kT_e \sim 0.2$ keV), is dominant along the rim, and is associated with the primary shock moving into the ISM and/or cavity wall. Since the shell is capturing the fresh ISM, it is in an ionizing phase (Miyata et al., 1994). The ionization timescale is around $10^{11} \text{ cm}^{-3} \text{ s}$ in the shell region. The second component, found in the interior of the SNR, shows higher temperatures ($kT_e \sim 0.7$ keV). The second component is metal rich, with Si:H ratios a few times solar (Uchida et al., 2009), implying that it arises at least in part from ejecta of the SN explosion.

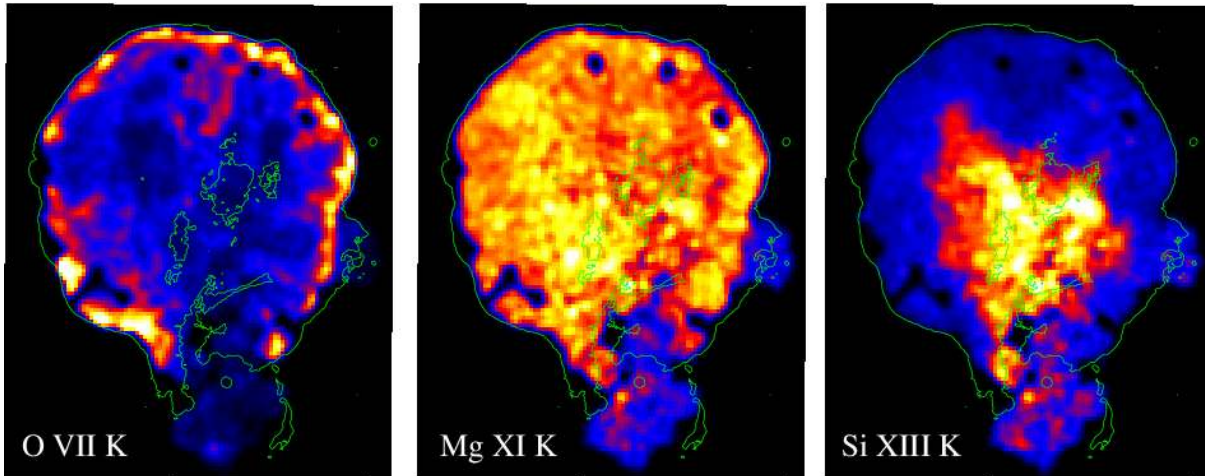


Figure 2: Equivalent width maps for $K\alpha$ lines of O VII, Mg XI, and Si XIII (Uchida et al., 2009). There are still some regions left unobserved with *Suzaku*, which appear as dark spots.

The first high resolution X-ray imagery of the Cygnus Loop was obtained with *Einstein* (Ku et al., 1984), and nearly complete maps of the remnant were made with *ROSAT* (Aschenbach & Leahy, 1999), *ASCA* (Miyata et al., 1998), *XMM-Newton* (Tsunemi et al., 2007) and *Suzaku* (Uchida et al., 2011, and references therein). Figure 1 (a) shows the X-ray image of the Cygnus Loop obtained with *ROSAT*. The the *ROSAT* HRI image mainly shows the low kT_e component of X-ray emission. The spectrum is dominated by emission lines from

various elements: O, Ne, Mg, Si, S, and Ar. The improved spectral resolution of X-ray CCDs made possible the production of images in some of these emission lines. Some *Suzaku* line images are shown in Figure 2. The O line dominates in the shell region indicating an ISM origin of the shocked gas there, while Si fills the interior indicating the hot ejecta component.

1.3.2 Cygnus Loop - Solving the low abundance problem

The basic question is what causes the “low abundance” problem. If abundances in the post-shock plasma are actually low, then accurate abundance measurements should provide an important clue as to the reason. On the other hand, if the problem arises due to physical processes that are not included in the standard analysis (of CCD data), then this should also be apparent.

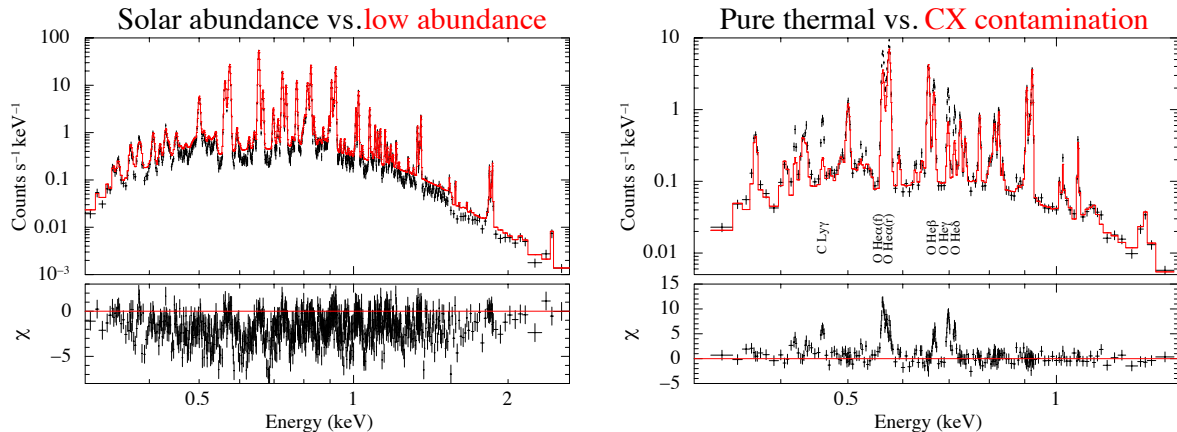


Figure 3: Left: Simulated 50 ks SXS spectrum for the northeastern region of the Cygnus Loop (the region is indicated by arrow 1 in Figure 1). Red and black correspond to the low abundance case (~ 0.2 solar) and the solar abundance case, respectively. The lower panel shows the residuals for the simulated data and the model for the low-abundance case. Right: Simulated 100 ks SXS spectrum for the northeastern edge of the Cygnus Loop (the region is indicated by arrow 2 in Figure 1). The simulated SXS spectrum includes contamination by CX emission, while the model represents pure thermal emission.

We first demonstrate that it is possible to accurately characterize the plasma with *ASTRO-H*. This is an important first step because by examining line strengths of individual lines we can verify whether the models applied to the CCD data are appropriate. For this, we simulate a 50 ksec observation of the bright northeast rim of the Cygnus Loop, as shown in Figure 1. To reduce the effects of CX emission, we select a region $\sim 6'$ inside from the outer rim. The left panel of Figure 3 shows a comparison between models with with low abundances (~ 0.2 solar) and solar abundances. Analysis of the simulated spectra shows that we can measure absolute abundances of C, N, O, Ne, and Mg individually to 10% accuracy (90% confidence level), something that is impossible with CCD spectra.

Secondly, to answer the question of whether atomic physics is the root cause of the apparently low abundances observed in the Cygnus Loop and other older SNRs, we need to obtain high-S/N and high-resolution observations of several positions along the rim of the Cygnus Loop. These observations are needed to fully characterize the spectrum, and to separate questions of abundances from those associated with other physical processes such as charge exchange and resonance scattering. Relatively short exposures in various regions of the Cygnus Loop with *ASTRO-H* can be used to evaluate the importance of these processes.

Resonance scattering changes the ratio of forbidden and resonance lines, and by reducing the intensity of the resonance lines can result in apparently lower abundances than is actually the case. An example of this is shown in Figure 4, which shows the escape probability for the O He-like resonance line at 0.57 keV in a plane of the O abundance and the turbulent velocity.

To demonstrate the ability of *ASTRO-H* to measure the effects of atomic processes that can affect abundance measurements, we have simulated short observations at two positions in the Cygnus Loop, one immediately

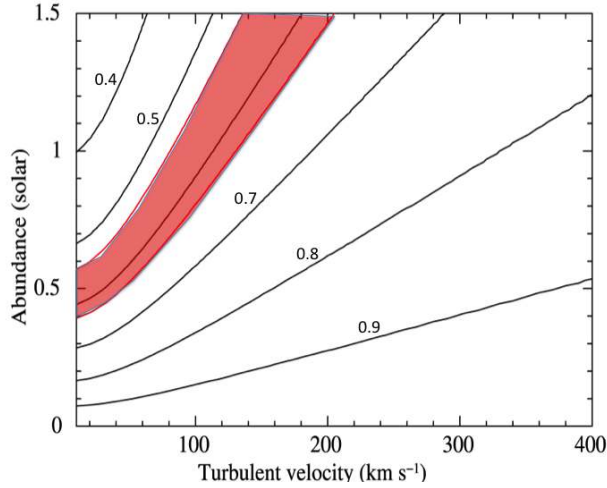


Figure 4: The escape probability of the resonance line in O He α (Z-axis) as a function of the O abundance (Y-axis) and the turbulent velocity (X-axis). The red area indicates a 90 percent confidence limit (statistical uncertainty) region for a 20 ks exposure time at the $0.95 R_{sh}$ position.

behind the shock and one slightly further in. Both positions are simulated assuming kT_e of 0.25 keV, an ionization age of $1 \times 10^{11} \text{ s cm}^{-3}$, and solar abundances. However, the line of sight column densities differ: $0.1 \times 10^{20} \text{ cm}^{-2}$ for the field at the edge, $0.25 \times 10^{20} \text{ cm}^{-2}$ for the interior field.

Our simulations show that we can accurately measure forbidden to resonance line ratios in both cases, to an accuracy of better than 10%, which will allow a direct assessment of the importance of resonance scattering in estimates of abundances in old SNRs like the Cygnus Loop. We also can distinguish between the case where charge exchange is important and not.

1.3.3 Cygnus Loop – Shock Cloud Interactions

The Cygnus Loop, Puppis A, and the Vela SNR provide nice examples of cloud-shock interactions. We here examine the so-called “XA knot” along the eastern edge of the Cygnus Loop, (see, Figure 1), where detailed optical and X-ray studies have been already performed (e.g., Danforth et al., 2001; Miyata & Tsunemi, 2001; Zhou et al., 2010; McEntaffer et al., 2011). As shown in Figure 1 (c), the knot shows a chaotic network of optical filaments, providing both edge-on and face-on views of shock fronts propagating into dense clouds. The speeds of the shocks have been estimated to be $\sim 100\text{--}200 \text{ km s}^{-1}$. Given this complex morphology, an SXS measurement of this region will sample a variety of shock speeds, yielding a spectrum suggesting random gas (bulk) motions of $\sim 400 \text{ km s}^{-1}$, i.e., $\pm 200 \text{ km s}^{-1}$. Moreover, plasma instabilities along the interface between the clouds and intercloud medium would yield additional turbulent velocities of $\sim 10\%$ of the shock speed (Pittard et al., 2010). Given these considerations, we would expect a random gas motion of at least $\sim 440 \text{ km s}^{-1}$, which causes line broadening of $\sigma \sim 1 \text{ eV}$ at O VIII Ly α (654 eV). We introduce this amount of broadening in the following SXS simulation for cloud-shock regions.

Here we demonstrate that *ASTRO-H* can be used to detect broadening in the lines. For this, we select the brightest area in the XA region, as shown in Figure 1 (b). To simulate SXS spectra, we first extracted an *XMM-Newton* MOS spectrum, and then fit it with a non-equilibrium ionization (NEI) plasma model. Based on the best-fit emission model, for which line broadening of 440 km s^{-1} (or $\sim 1 \text{ eV}$ at 654 eV) estimated above is taken into account, we simulate an SXS spectrum as shown in Figure 6. Due to the brightness of this region, an exposure time of only 20 ks allows us to collect $\sim 13,000$ counts in 0.2–2 keV. In the right panel of Figure 6, we show a close-up spectrum for O K-shell lines, in which we show an emission model (in red) having no line broadening (i.e., the broadening is solely due to instrumental resolution). It is clear that the simulated spectrum has broader lines than the model, and thus we can measure the line widths (and turbulent velocities in the region) within about 10% accuracy. It should be noted that detecting such minor broadening will require

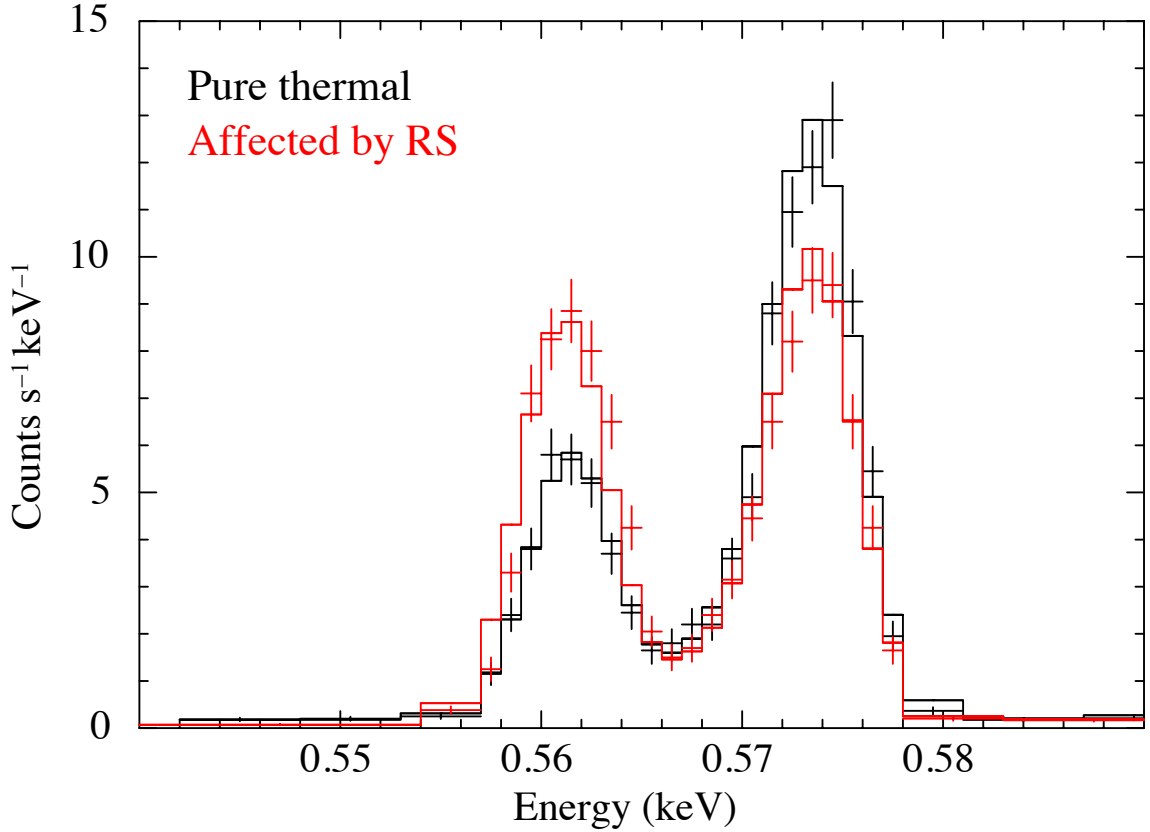


Figure 5: A 30 ks simulation of the NE limb of the Cygnus loop, somewhat inside the shock (at R/R_s of 95%), showing the effects of resonance scattering on the spectrum. The black data points are for a model in which charge resonance scattering is ignored; the red points include the effects of resonance scattering.

that the SXS spectral resolution is very well calibrated.

1.3.4 Cygnus Loop – Nature of the progenitor

Preite Martinez (2011) argue, essentially on energetic grounds, that the Cygnus Loop was the result of explosion of a relatively low ($8\text{--}10 M_\odot$) mass star, which produced a SN of low energy, possibly an electron-capture SN. On the other hand, Uchida et al. (2011) argue from *Suzaku* spectra that abundances of Ne, Mg, and Si relative to O are better understood in terms of a $12\text{--}15 M_\odot$ progenitor. Using *ASTRO-H*, it will be possible to accurately measure the metal abundances for direct comparison with models such as those of Woosley & Weaver (1995).

Figure 7-left shows a 100 ks SXS simulation of the center of the Cygnus Loop. The emission here consists of three components. Blue and magenta show two shell components, near side and far side, respectively. Red shows the ejecta component while the black shows the sum. As shown in Figure 7-right, the spectrum above 1 keV mainly comes from the ejecta component.

Although we cannot separate the motion between the near side shell and the far side shell, the O VIII line width of might provide a measure of the expansion velocity. The Si XIII triplet will be resolved, allowing us to determine the plasma conditions. The simulation shows a representative interior pointing.

1.3.5 Vela SNR - Background

Another old ISM-dominated SNR that is important to study is the Vela SNR. It is a textbook example of an evolved core-collapse SNR, exhibiting overwhelming soft X-ray emission from blast-wave shocked clouds (e.g., Lu & Aschenbach, 2000), underlying relatively-faint line emission from metal-rich ejecta (e.g., LaMassa

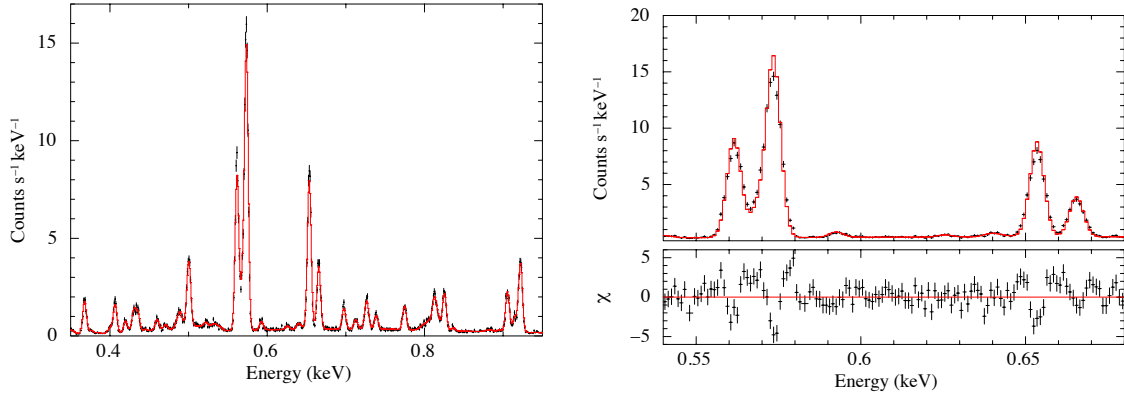


Figure 6: Left: Simulated 20 ks SXS spectrum for the XA region of the Cygnus Loop. Right: Close-up of the SXS spectrum in the left panel, but with the best-fit model having no line broadening, i.e., only instrumental broadening. The lower panel shows residuals. It is clear that the line profiles in data are broader than those in the model.

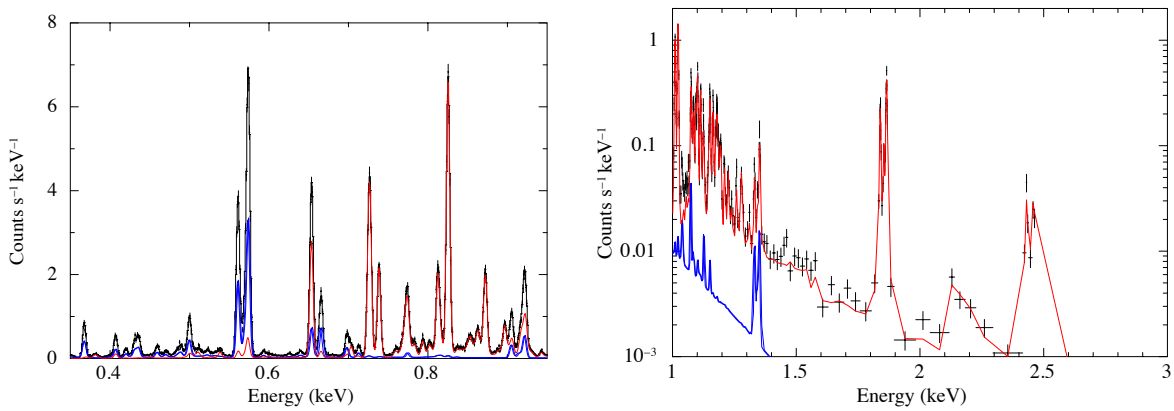


Figure 7: Simulation of a 100 ks SXS observation of the interior of the Cygnus Loop. Left shows the spectrum below 1 keV where blue and magenta show two shell component: near side and far side. Red shows the ejecta component. Right shows the spectrum above 1 keV where ejecta the component dominates.

et al., 2008), and interaction between an expanding pulsar wind nebula and a confining reverse shock (e.g., Blondin et al., 2001). In addition, there are a few isolated structures called “shrapnel” beyond the forward shock, which are identified as ejecta fragments by their strong line emission by metals thought to be ejecta (e.g., Katsuda & Tsunemi, 2005).

Figure 8 shows SXS simulations of three representative regions: north (30 ks), center (100 ks), and shrapnel D (80 ks), which are intended to indicate the breadth of studies that can be carried out in the Vela SNR. The exposure times are chosen so that statistics for the spectra are roughly the same. The thermal spectra within the main body of the Vela SNR are generally well described by a two-temperature model (Lu & Aschenbach, 2000). The low-temperature plasma (blue in the simulation spectra) arises in the shock-heated ISM clouds that dominate the ROSAT image shown in top-left panel of Figure 8, while the high-temperature plasma (red in the simulation spectra) originates from either the evaporation of shocked clouds, ejecta or a mixture of the two (Miceli et al., 2006). *ASTRO-H* spectra are needed to advance our understanding of the physical processes and abundances in each of these regions.

The north region is dominated by the soft X-ray emission arising from the interaction between the blast wave and ISM clouds (e.g., Miceli et al., 2005). Its high surface brightness will allow the obtaining of high S/N spectra with relatively short exposures. Although extensive CCD-based studies have explored cloud–shock interactions within this region (Lu & Aschenbach, 2000; Miceli et al., 2005, 2006), its low temperature (~ 0.1 keV) has hampered detailed plasma diagnostics to date, because the emission lines, mostly below 0.5 keV.

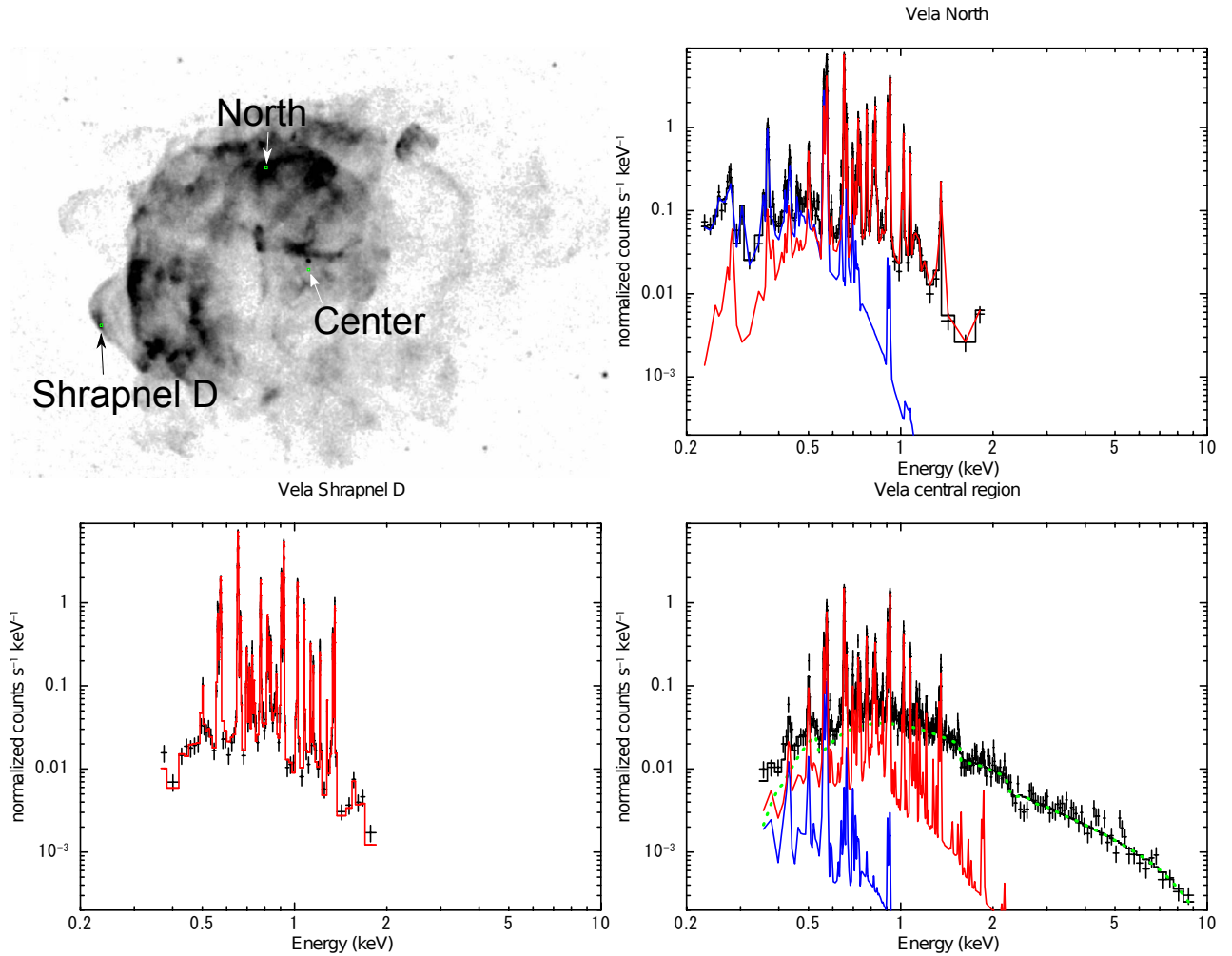


Figure 8: **Top-left:** The ROSAT All-Sky Survey image of the Vela SNR. The north, shrapnel D, and center regions, for which we perform SXS simulations, are shown with green boxes. **Top-right, bottom-left, and bottom-right:** The SXS simulations of the north, shrapnel D, and center regions. Red, blue, and green lines represent the high-, low-temperature, and non-thermal plasma models, respectively.

The *ASTRO-H* SXS will isolate C, N, and O lines for the first time and thus provide new insight into the dynamics and plasma conditions in the shock-heated clouds.

The central region of the Vela SNR contains not only soft X-ray emission from shocked clouds, but also line emission from metal-rich ejecta and non-thermal emission from the pulsar wind nebula (LaMassa et al., 2008; Katsuda et al., 2011). Since the ejecta at the center of the remnant is expected to be less contaminated by ISM in comparison with those at the shell, observations of this plasma will allow *ASTRO-H* to study the abundance pattern in the ejecta, which is needed for better understanding of the progenitor. However, in most locations, other thermal and non-thermal components coexisting in projection partially hide or dilute the ejecta emission. As a result, observations of the almost purely ejecta-dominated shrapnel D region are critical. The SXS will determine with unprecedented precision the plasma conditions in both shrapnel D and the high-temperature component in the central region, thereby allowing efficient extraction of abundance information. These measurements will allow us to determine whether the high velocity ejecta overrunning the blast wave and the slow velocity ejecta in the interior originate from the same progenitor layer, thus shedding light on the explosion mechanism.

Given Vela's age (over 10,000 yr), an interaction between the pulsar wind nebula and the reverse-shock is expected to have occurred (Blondin et al., 2001). The filamentary structure of the radio morphology is highly

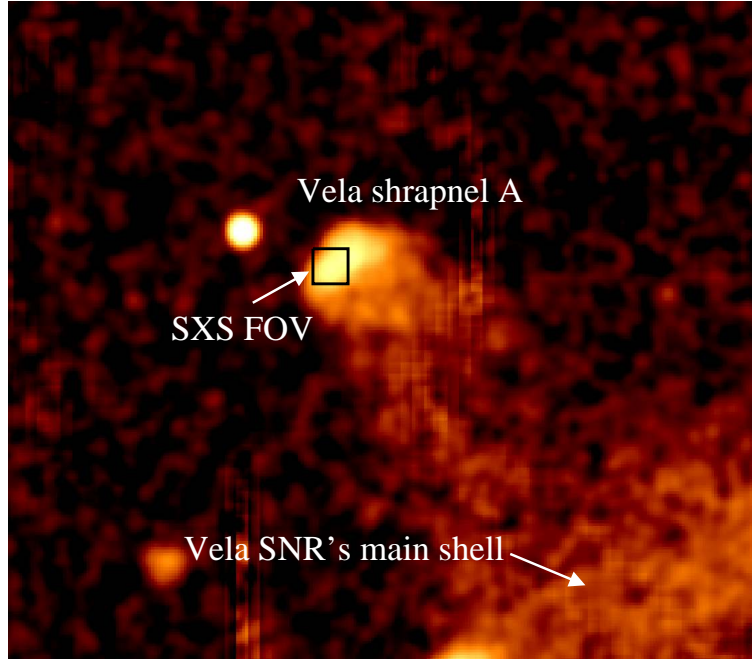


Figure 9: ROSAT All-Sky Survey image of Vela shrapnel A. The SXS FOV is shown as a black box.

suggestive of mixture of two different fluids, namely pulsar wind and ejecta (Bock et al., 1998). The situation where the strong magnetic fields, $\sim 100 \mu\text{G}$ at least around the bright PWN (Pavlov et al., 2003), and the thermal plasma interact with each other may produce a supra-thermal electron distribution, deviating from Maxwellian (Masai et al., 2002; Kaastra et al., 2009). The supra-thermal electrons will change the relative intensities of the satellite lines (Kaastra et al., 2009), which may be tested with the SXS spectrum.

1.3.6 Using velocity-broadening to measure ejecta metallicity in the Vela SNR through observations of “shrapnel”

A number of older SNRs, including Vela, show evidence of metal-rich plasmas, and are worthy of study with *ASTRO-H*. To date, we have only lower limits on the abundances for such high-metallicity plasmas. As we have discussed above, with the *ASTRO SXS* we will be able to carry out straightforward abundance studies of many of these SNRs, and this will be very important to determining the nature of the progenitor of these objects. However, *ASTRO-H SXS* also enables a different kind of test of the amount of overabundance by using the width of the lines to estimate the post-shock ion temperature of the gas after Coulomb equilibration, which depends on a combination of the shock speed and the metallicity.

The Vela SNR’s Shrapnel A, which is a relatively compact, Si-rich ejecta knot (see, Figure 9), provides the best place to pursue such an observation. The basic idea is as follows: For a fixed shock speed, all elements have the same initial shock-heated temperatures which are proportional to their elemental masses (in collisionless shocks). However, the temperature evolution due to Coulomb equilibration depends on the metallicity. For fixed shock speed, the temperature of the plasma is much higher in the case with pure metals than one with a mixture of H and heavier metals. For example, as shown in Figure 10, for an assumed shock velocity of 2000 km s^{-1} (which is a mean velocity, radius/age, for Vela Shrapnel A), the ion temperature is expected to be about 200 keV for a pure metal case, but only 7 keV for a several-solar case. The temperature of either 200 keV or 7 keV would result in line broadening of either $\sigma = 2.4 \text{ eV}$ or 0.44 eV , respectively, at the ionization timescale in Vela A ($(n_e t \gtrsim 10^{11} \text{ cm}^{-3} \text{ s}$: Tsunemi et al., 1999; Miyata & Tsunemi, 2001; Katsuda & Tsunemi, 2006). Such a difference can be easily distinguished by the SXS with a 200 ks exposure, for which the SXS simulation is presented in Figure 10, hence we will be able to determine the absolute metallicity there.

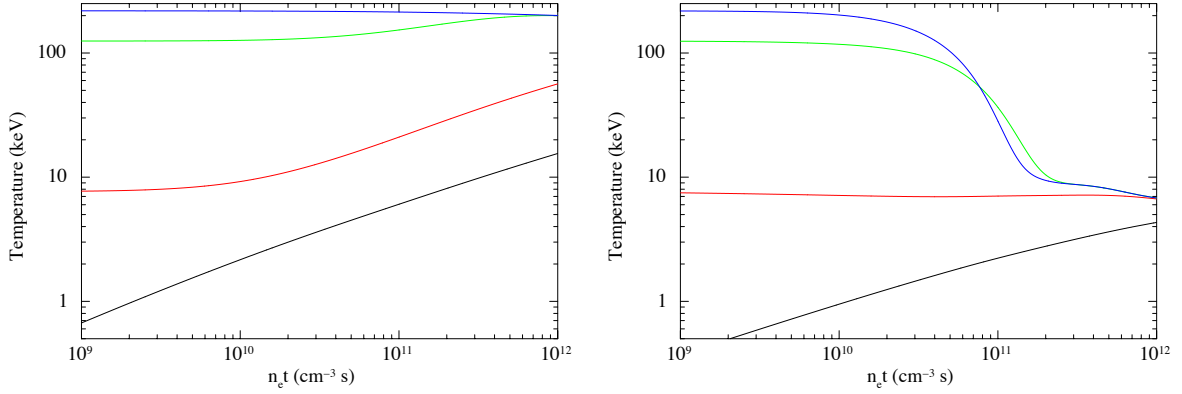


Figure 10: left: Temperature histories for electrons (black), protons (red), oxygen (green), and silicon (blue) as a function of the ionization timescale. In the calculation, we assume that the plasma is (nearly) pure metal abundances and that temperature equilibration takes place through only Coulomb interactions after collisionless shock heating ($V_{shock} \sim 2000 \text{ km s}^{-1}$). right: Same as left but for a slightly elevated abundance (several-solar abundance) plasma.

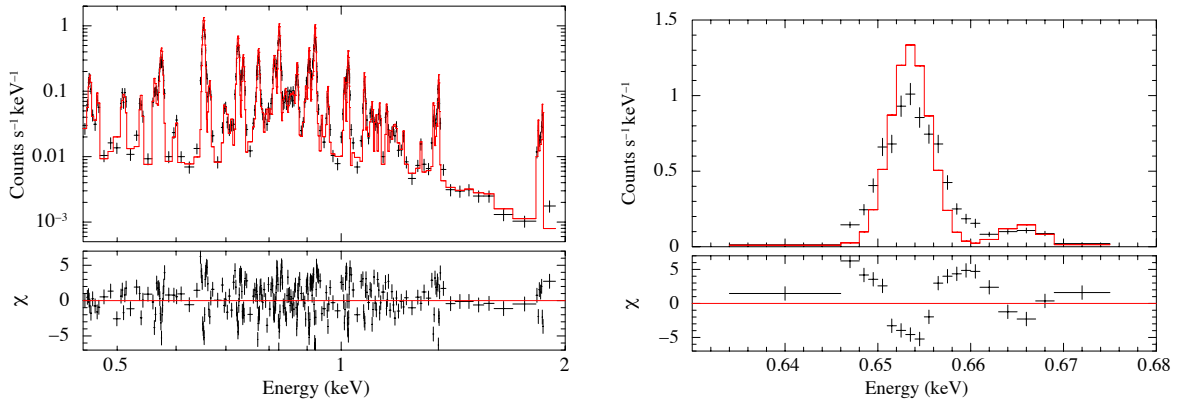


Figure 11: Left: Simulated 200 ks of Vela A with SXS. The simulated data in black assume a pure metal case, while the model curve in red assume several solar abundances. Right: Close-up of the O Lyman band. We can measure the line width to be $2.4 \pm 0.2 \text{ eV}$.

2 Mixed-Morphology Supernova Remnants

2.1 Background and Previous Studies

There exists a substantial population of old SNRs displaying centrally peaked X-ray emission arising from thermal plasma (White & Long, 1991; Rho & Petre, 1998). These remnants generally appear shell-like in the radio, hence the name mixed-morphology SNRs (Rho & Petre, 1998). They are generally found near dense interstellar structures, usually molecular clouds, often interacting with them. A large fraction contain OH masers (Yusef-Zadeh et al., 2003).

Recent studies of mixed-morphology SNRs have revealed three important new features. At least one-third of these SNRs have associated γ -ray emission (see, e. g. Vink, 2012). This emission is thought to arise from relativistic protons, originally accelerated in the magnetic field of the forward shock, colliding with material in the nearby molecular clouds. The resulting γ -ray emission is the strongest evidence favoring cosmic ray acceleration in SNR shocks. A second recently discovered feature is the presence of enhanced metal abundances in the interiors of about half the known mixed-morphology SNRs (Lazendic & Slane, 2006; Shelton et al., 2004). These enhanced abundances suggest that ejecta has not completely mixed with the surrounding ISM, despite the fact that most are of these SNRs are thought to be relatively old ($>20,000$ years), and that many are in the radiative phase. Third, while early studies of these remnants indicated their X-ray emitting plasma is close to collisional ionization equilibrium (Rho & Petre, 1998), observations using *ASCA* and *Suzaku* have revealed

surprisingly that some contain over-ionized and thus recombination-dominated plasma (RP), evidenced by both line ratios (Kawasaki et al., 2002) and radiative recombination continua (RRCs: Yamaguchi et al. 2009).

The mechanisms responsible for forming mixed-morphology SNRs are still not completely understood. The absence of an X-ray shell suggests that these remnants are dynamically old, and that the forward shock has slowed down to a velocity too slow to produce substantial X-ray emission above ~ 1 keV. However, most of these remnants are observed through high column density ($1\text{--}2 \times 10^{22}$ cm $^{-2}$), so X-ray emission from a shell produced by a forward shock with velocity less than a few hundred km s $^{-1}$ would be absorbed. However, the only known Galactic mixed-morphology remnant with a low intervening column, G65.3+5.7, shows a shell only below ~ 0.5 keV, supporting the idea that mixed-morphology remnants have evolved to an evolutionary phase later than the old shell-like SNRs typified by the Cygnus Loop. Indeed, some are thought to have entered the radiative phase (Shelton et al., 2004).

White & Long (1991) suggested that the centrally enhanced emission arose from clouds bypassed by the primary shock due to their high density, which subsequently were evaporated by hot gas in the interior. Their simple self-similar model for the evolution of such SNRs, which predicts younger ages and lower swept up masses than a Sedov-based single component ISM analysis, is almost certainly incorrect in detail, but whether evaporating clouds contribute to the interior gas density is less clear. Shelton et al. (1999) suggested instead that a SNR expanding into a dense ISM with a strong decreasing density gradient, coupled with thermal conduction or turbulent mixing, was more likely to produce the observed morphology. Neither model includes the possibility that emission from ejecta could contribute to the X-ray morphology of these SNRs.

Recent *Suzaku* study of mixed-morphology SNRs (Yamaguchi et al., 2012; Sawada & Koyama, 2012; Uchida et al., 2012) suggests that a specific sequence of events could be responsible for producing the RP. The shock from a supernova exploding in a dense circumstellar medium (CSM), presumably formed by a pre-supernova wind, would rapidly heat both the CSM and ejecta to a high temperature (kT_{high}). The high density causes the plasma to rapidly approach collisional ionization equilibrium. As the forward shock expands beyond the CSM envelope, the shock rapidly accelerates. The shocked material becomes rarified and cooled (kT_{low}), and if the adiabatic cooling timescale of the electrons is shorter than the recombination timescale of the ions, then an over-ionized plasma is formed. It can persist for a long time, while gradually relaxing (recombining) to reach collisional ionisation equilibrium at kT_{low} .

This model, originally proposed by Itoh & Masai (1989), raises as many questions as it purports to solve, many of which are testable. It requires a specific pre-SN wind structure, and thus only progenitors in a specific mass range would produce mixed-morphology remnants. It is not clear how the ejecta remain centrally concentrated, although some idea has been proposed to explain the morphology as well (Shimizu et al., 2012). Perhaps more importantly, all mixed-morphology remnants are dynamically old; where are the early stage mixed-morphology remnants and where are the dynamically old remnants from outside this mass range? Given the morphological complexity of these remnants and their environments, it is likely that no single model works, and rarefaction, conduction, and evaporation (and possibly other mechanisms) all contribute.

2.2 Prospects & Strategy

There are two primary objectives in studying mixed-morphology SNRs using *ASTRO-H*. The first is a thorough study of the over-ionized plasmas. The SXS will provide powerful plasma diagnostics, allowing us to carefully measure line ratios from a variety of metals, and therefore better quantify the ionization conditions. For remnants in which strong RRCs have been detected, it can be used to precisely measure known RRCs and sensitively search for RRCs from different metals. SXS measurements will allow us to determine whether the over-ionization conditions vary across a remnant. Additionally they will enable a more sensitive search for RRCs and line ratios indicating over-ionization in remnants where these features have not been detected.

The second objective is to more accurately characterize the abundances and distribution of the ejecta observed towards the centers of many mixed-morphology remnants, with the goal of establishing progenitor masses. The relationship between the presence of over-ionization and enhanced abundances will provide clues about the progenitor and the conditions responsible for forming mixed-morphology SNRs.

Both objectives have the potential to provide new insights into the origin and evolution of this class of SNRs. A carefully constructed observing program can fulfill both objectives with a common set of observations, especially as several mixed-morphology SNRs show both traits. Most of these remnants are much larger than the SXS field of view and have relatively low surface brightness. Complete mapping in general would not represent a productive use of *ASTRO-H* time. However, all have been mapped using previous missions, and these maps can be used to define a small set of pointings for each remnant of interest.

If the rarification scenario is correct, then understanding the early evolution of the plasma is critical as it would naturally be related to the explosion mechanism and environment of mixed-morphology SNRs. The SXS enables independent determination of key parameters associated with the initial explosion environment and subsequent evolution, namely the electron temperatures before and after the cooling (kT_{high} and kT_{low}) and the recombination age ($n_e t$) of the later relaxation phase.

Additionally, the elemental dependence of ionization states is crucial for determining the conditions responsible for initially producing the RP. Fe ions require high temperature above 10 keV to be fully ionized, while the lighter elements can reach the full ionization with ~ 1 keV. If Fe ions have higher ionization states than others, that means the RP has higher kT_{high} .

2.3 Targets & Feasibility

2.3.1 W49B

W49B is probably the youngest Galactic mixed-morphology remnant. While showing both RP and enhanced abundances (Ozawa et al., 2009), it has by far the highest temperature of any mixed-morphology remnant. It is surrounded by dense molecular clouds, which are probably responsible for shaping both its morphology and for producing its rapid evolution. It has been classified as both a Type Ia and a core collapse remnant. It shows enhanced metal abundances, and, crucially, is the only mixed-morphology remnant showing strong Fe K lines. W49B is 4×3 arcmin², and unlike most Galactic mixed-morphology SNRs, could be completely mapped using a small number of SXS pointings. While the metal distribution has been well characterized using *Chandra*, the degree of over-ionization has not been mapped.

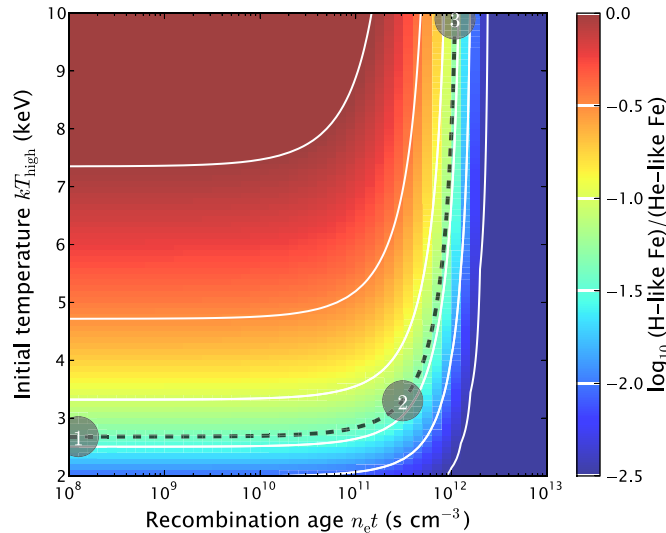


Figure 12: Contour map of Fe-K H/He ionic abundance ratio calculated with SPEX. *Suzaku* constrained region for W49B is shown in the dashed line. We cannot resolve the initial temperature kT_{high} or the recombination age $n_e t$. We have calculated 3 model spectra for W49B with assumptions about the initial temperature and recombination age indicated by the 3 large dots.

As discussed in Section 2, the underlying physical mechanisms causing over-ionization in mixed morphology

SNRS are a mystery. We do not know whether the plasma in these systems is heating or cooling, or whether the recombination age is short or long, since with CCDs one can only resolve the H and He-like lines in the spectra. Consequently, we do not know whether the mechanism that leads to cooling is rarefaction, conduction, or some other process.

W49B is the best object for addressing some of these questions. The *Suzaku* constraints on the initial temperature and recombination age are shown in Figure 12. The initial temperature could range from 2.7 keV to higher than 10 keV, and the recombination age could range anywhere from less than 10^8 s cm^{-3} to 10^{12} s cm^{-3} .

W49B is especially important because of the diagnostic power provided by the Fe-K lines. The fine structure of the Fe-K line complex provides the best information about the evolutionary stage of RP (as a function $n_e t$). The longer recombination age results in a broader ion population. The SXS can resolve Fe $K\alpha$ lines into Ly- α , He-like triplets, and satellite lines from lower ionization states. Their flux ratio provides a direct measure of the ion population.

To show the diagnostic capability of *ASTRO-H* SXS, we have carried out a set of 200-ks simulations of the W49B spectrum corresponding to three different assumptions, covering the wide range of potential initial temperatures and recombination ages. Model 1 has an initial temperature of 2.7 keV and a short recombination age, model 2 has a temperature of 3.3 keV and an age of $10^{11.5}$ s cm^{-3} , and model 3 has a temperature of 10 keV and an age of 10^{12} s cm^{-3} . As shown in Figure 13, one very clear way to determine these parameters is from the satellite lines, which increase in strength with the recombination age.

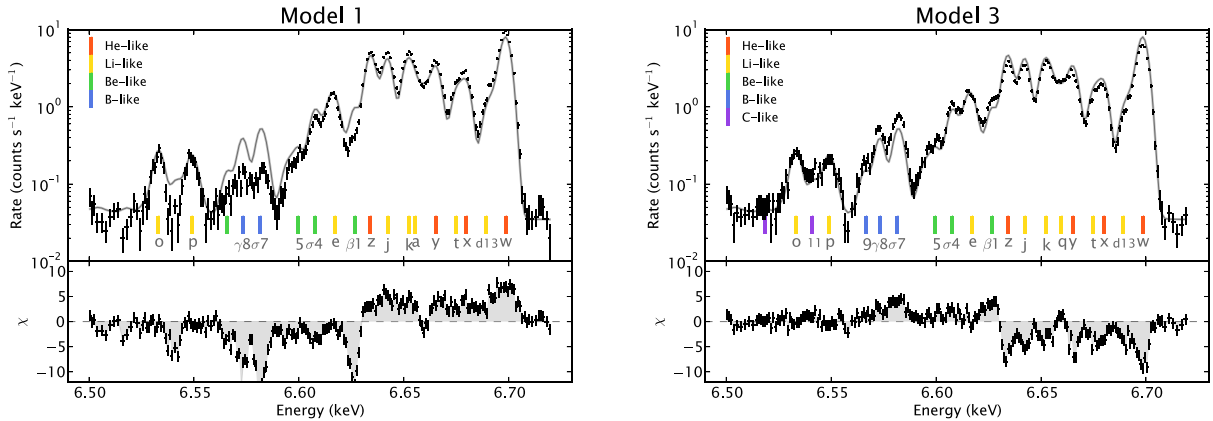


Figure 13: Upper panels: 200-ks simulation results of Fe- $K\alpha$ line of W49B with SPEX, with the assumptions for models 1 and 3 (crosses). The lower panels show the differences between these spectra and that predicted for model 2 (faint curves in the upper panels). The differences in the 3 models are associated with changes in the intensities of the satellite lines.

Similarly, *ASTRO-H* SXS observations could potentially distinguish between the main two explanations for over-ionization, namely rarefaction or conduction. If the plasma is cooled by rarefaction (adiabatic expansion), then high density and high initial temperature are required, which in turn implies ion-electron temperature equilibrium ($kT_i = kT_e$). However, if recombining plasmas are produced by conduction, then the process of cooling will cause electrons to cool faster than ions, and thus $kT_i > kT_e$. In this case, temperatures measured from thermal broadening will exceed those derived from line ratios and continuum emission. *ASTRO-H*, with SXS, will be able to detect this, as shown in Figure 14 in the same 200 ks required to measure the satellite lines.

2.3.2 Other potential targets

W44 is the prototypical mixed-morphology SNR. It shows all the class traits, including OH masers, gamma-ray emission, enhanced central abundances, and RP. It is relatively large (35×27 arcmin) so a complete SXS mapping is not possible. To determine the extent of the RP and the distribution of metals, a series of order 5 pointings is envisioned, one at the center and one off set in each of the cardinal directions.

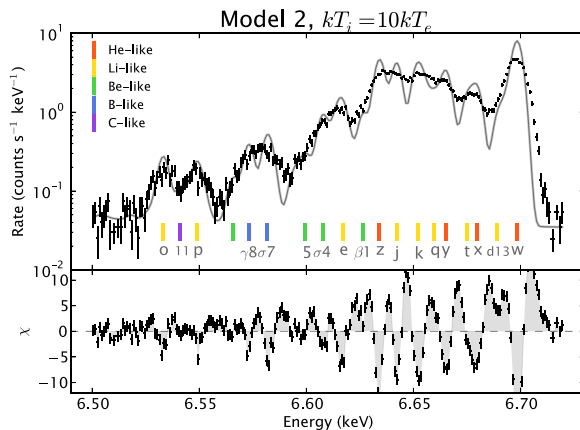


Figure 14: Same 200-ks simulation with SPEX, but with thermal broadening in case of model 2 (crosses). We assumed $kT_i = 10kT_e$ in the simulation.

IC 443 is typically not classified as a mixed-morphology SNR, but shares many features with the class. It is interacting with an H I cloud to its east and with a thin molecular cloud along the line of sight. The highest surface brightness arises in the interior, adjacent to the two cloud interaction regions, and there is a hint of a shell in some locations around the periphery. The bright region shows enhanced metal abundances and is where the first evidence of over-ionized plasma in any SNR was found using *ASCA*, and the first strong RRC was found using *Suzaku*. It is possible that IC 443 represents a remnant in the process of transition into a mixed-morphology remnant.

3C 391, another prototypical mixed-morphology remnant, shows a clumpy interior with a lack of spectral variation (except for a column density gradient). It shows neither evidence for ejecta nor RRC features. One pointing could thus serve as a "control" for other measurements of mixed-morphology remnants, or it could reveal the presence of enhanced abundances and/or RP.

G65.3+5.7 is the nearest mixed-morphology remnant, and the one with the lowest column density. Its very large diameter (4×5 degrees) makes mapping impossible. It is the only mixed-morphology remnant whose forward shock can be observed.

2.4 Beyond Feasibility

As evolved SNRs, mixed-morphology remnants are not expected to emit the non-thermal hard X-rays characteristic of relativistic electrons, and hard non-thermal tails are typically not detected from them. Their age relative to the electron synchrotron cooling time is too old to expect the presence of the TeV electrons responsible for the synchrotron emission seen from the forward shocks of young SNRs. On the other hand, the detection of γ -ray emission from many mixed-morphology remnants indicates that acceleration did occur at one time. The HXI will provide the most sensitive measurements for non-thermal emission above 10 keV for many of these objects, and either stringent limits on acceleration parameters or a surprise detection.

3 Pulsar Wind Nebulae and their Evolution

3.1 Background and Previous Studies

While type Ia supernova explosions involving the nuclear detonation of a white dwarf do not lead to the formation of a compact stellar remnant, core-collapse explosions of massive (≥ 8 solar masses) stars give birth to some of the most dense and magnetic stars in the Universe: neutron stars¹. Following their birth, these compact

¹The most massive stars are commonly believed to form black holes not discussed in this white paper.

objects powered initially by their fast rotation spew out a relativistic wind of particles and fields (called pulsar wind) which, as it interacts with the surrounding medium, gets shocked leading to the formation of a pulsar wind nebula (PWN). PWNe have been observed to emit non-thermal radiation across the electromagnetic spectrum from radio to the highest energy gamma-rays. Their emission, often located near the supernova explosion site (at least in the early phases of the SNR evolution), gives the SNR a centrally-filled morphology, thus their other name “plerions” (for the ancient greek word *pleres*: $\pi\lambda\eta\rho\eta\varsigma$). If the neutron star was given a velocity kick at birth, then, as the SNR ages, the neutron star and associated PWN can move away from the SNR center and eventually interact with and leave the SNR shell.

As the synchrotron bubbles inflated by fast-spinning, highly magnetized, neutron stars, PWNe provide nearby laboratories to study the physics of relativistic shocks, their interaction with their hosting SNRs, and to search for the missed pulsars in our Galaxy and beyond. They are also believed to accelerate cosmic rays to TeV energies. Recent reviews on PWNe can be found in Gaensler & Slane (2006) (on their structure and evolution), Slane (2008); Kargaltsev & Pavlov (2010) (on their high-energy emission), and Safi-Harb (2012, 2013) (on recent statistics and the growing class of atypical PWNe).

The most famous and best studied PWN is the Crab Nebula, whose progenitor exploded in AD 1054, and which provided the first confirmation of Baade & Zwicky’s 1934 prediction that neutron stars are born in supernovae (see Hester, 2008, for a review of its properties). Moving outward, the Crab nebula consists of a 33-ms rotation-powered pulsar, a bright synchrotron nebula observed across the electromagnetic spectrum, bright filamentary ejecta observed in the optical, and a faint freely expanding supernova remnant. Despite deep searches, the outer shock associated with the blast wave of the SNR remains undetected (Seward et al., 2006), making the Crab nebula a “pure plerion” or filled-centre SNR. Other SNRs however have a composite-type morphology arising from the pulsar-powered (or plerionic) component plus an outer shell representing the location of the blast wave. Such SNRs are referred to in the literature as plerionic Composites. Out of the 314 known SNRs, we know of ~ 90 SNRs harbouring PWNe (Green, 2009; Ferrand & Safi-Harb, 2012).

PWNe are initially confined by the supernova ejecta (as in the Crab nebula), but as they evolve their dynamics become affected by the circumstellar or interstellar medium. At any stage of PWN evolution, their X-ray emission provides a unique window to probe the freshly injected particles accelerated at the PWN shock and the interaction with the SNR material. The *Chandra* X-ray observatory in particular has provided us with a high-resolution view of these objects, allowing us to study for the first time their fine structure, dynamics, evolution, and pulsar wind properties (Kargaltsev & Pavlov, 2008).

Even some 45 years after the discovery of the Crab and Vela pulsars in their respective SNRs, we do not know yet why dozens of PWNe lack the shells expected from the supernova explosion (like the Crab) while others are clearly surrounded by SNR shells (like Vela). Are the missing shells associated with a too-low ambient density, and if so, can we infer their progenitors? Is the explosion mechanism different among these seemingly different classes of objects? What role does their evolutionary stage (or age) and ambient conditions play in shaping their morphology and multi-wavelength emission? And why do some SNe form PWNe, others magnetars, and still others neutron stars with low magnetic fields? The lack of observed thermal X-ray emission from these synchrotron-dominated sources remains of the biggest puzzles in this field.

Furthermore, very little is known about their X-ray spectra above ~ 10 keV. Being hard X-ray sources with spectra characterized by a power-law with a nearly flat photon index, their synchrotron emission is expected to extend into the hard X-ray band (100’s of keV) with a break that could be associated with synchrotron losses. Furthermore, their 0.5–10 keV X-ray spectra appear to be systematically harder than those of their TeV counterparts (Kargaltsev & Pavlov, 2010). Studying the broadband spectrum in the 0.5–600 keV band (*ASTRO-H*’s range) will fill the gap between the lower energy studies and the gamma-ray studies, thus shedding light on their magnetic field, ambient density, and acceleration process (Reynolds, 2009; Gaensler & Slane, 2006). In particular, gamma-ray studies with H.E.S.S. have opened a new window to study the more evolved objects through the detection of offset PWNe believed to be “relic” nebulae resulting from the interaction with the SNR reverse shock, as e.g. for Vela (Aharonian et al., 2006); see also Blondin et al. (2001). Such multi-wavelength studies are, for the first time, addressing the leptonic versus hadronic models for pulsar winds, shedding light on their composition and other intrinsic properties such as their magnetic field.

3.2 Prospects & Strategy

Thanks to the unprecedented sensitivity and spectral resolution of SXS on board *ASTRO-H*, we will be able to address the missing SNR shell problem and search for signatures of the X-ray emitting ejecta in the pure or shell-less plerions. As an example, after accumulating ~ 500 ks of *Chandra* time on the “Crab-like” PWN G21.5–0.9, long thought to be a similarly young and a pure plerion, a limb-brightened X-ray feature (SNR blast wave candidate) as well as thermally emitting “knots” (ejecta candidate) were found, making G21.5–0.9 a textbook example of a young plerionic Composite-type SNR (Matheson & Safi-Harb, 2010, 2005; Bocchino et al., 2005; Safi-Harb et al., 2001; Slane et al., 2000). X-ray studies of a handful other PWNe with *Chandra*, *XMM-Newton* and *Suzaku* have shown evidence for extended thermal X-ray emission, that could be associated with the shock-heated ejecta or the missing SNR shell, beyond the known plerions in 3C 58 (Gotthelf et al., 2007; Slane et al., 2004) and G54.1+0.3 (Bocchino et al., 2010).

Furthermore, the unique broadband coverage of *ASTRO-H* in the 0.5–600 keV will provide broadband spectra of PWNe, filling the gap between soft X-ray spectra (with current missions) and the gamma-ray spectra (with *Fermi* in the GeV and H.E.S.S. in the TeV), allowing us to search for spectral breaks in the hard X-ray band.

PWNe are also highly polarized sources. Polarimetric measurements of the brightest objects with the SGD and potentially HXI will open a new window to study the magnetic fields in PWNe.

3.3 Targets & Feasibility

The relatively small size of PWNe (\leq arcminutes-scale) makes them excellent targets for SXS. However the relatively poor imaging resolution of SXS and high non-thermal brightness of PWNe (in comparison to any thermal emission associated with the SNR shell or ejecta) make the detection of any hidden thermal emission challenging. To achieve this latter potentially ground-breaking scientific goal, off-pulsar SXS pointings will have to be optimized to maximize the detection likelihood of the thermal emission, while minimizing any contamination by the non-thermal emission from the pulsar and PWN. Here we discuss two young targets that are strong candidates for the study of thermal X-ray emission from PWNe, but that require SXS’s spectral resolution and sensitivity to shed light on the nature of this emission and thus on their supernova progenitors and environment.

3C 58 is an excellent target to advance our understanding in this area. 3C 58 is sufficiently extended that direct contamination from the pulsar can be avoided. Using *XMM-Newton*, Gotthelf et al. (2007) detected soft (~ 0.2 keV) thermal emission throughout the SNR, and concluded that Ne was likely several times solar. However, with the limited spectral resolution of *XMM-Newton*, it was not possible to separate out other elements or probe the dynamical properties of the ejecta.

Figure 15 shows two 100-ks SXS simulations of 3C58 using *simx*. To begin these simulations, we used the archival *XMM-Newton* data and extracted a spectrum from the region $2'.5$ south-west from the pulsar, where the thermal flux is highest while the bright non-thermal central nebula can be avoided (Gotthelf et al., 2007). The solar abundance model, except for elevated Ne, provided a satisfactory fit as previous works. As noted in Gotthelf et al. (2007), we stress that this abundance pattern might be interpreted to be an ISM-origin, not an ejecta-origin, considering recent updates of ‘solar-abundance’ in which the Ne abundance is systematically increased (Drake & Testa, 2005; Cunha et al., 2006). On the other hand, the *XMM-Newton* CCD spectrum also allowed a fit with the abundance pattern that is calculated from a $18 M_{\odot}$ -progenitor mass case (Woosley & Weaver, 1995), where Ne/O is slightly enhanced while Fe/O is depleted compared to the solar ratios. Figure 15 shows such two different cases, we tentatively call them as the ISM and ejecta cases, which CCD-type resolution can not distinguish but the SXS can. Contamination of non-thermal emission from the bright central region is appropriately taken into account. Although absolute abundances are still difficult to be measured because the thermal continuum is mostly buried under overwhelming non-thermal emission, the relative abundances between O, Ne, Fe, and possibly Mg as well as the electron temperature and ionization timescale can be obtained with a ~ 10 – 20% accuracy (50% for Mg/O), which allows us to precisely estimate the progenitor type and the plasma conditions. Furthermore, we note that the line broadening may be more efficient to discriminate the two cases (see insets of Figure 15). Given the young age of 3C58 (suggested to

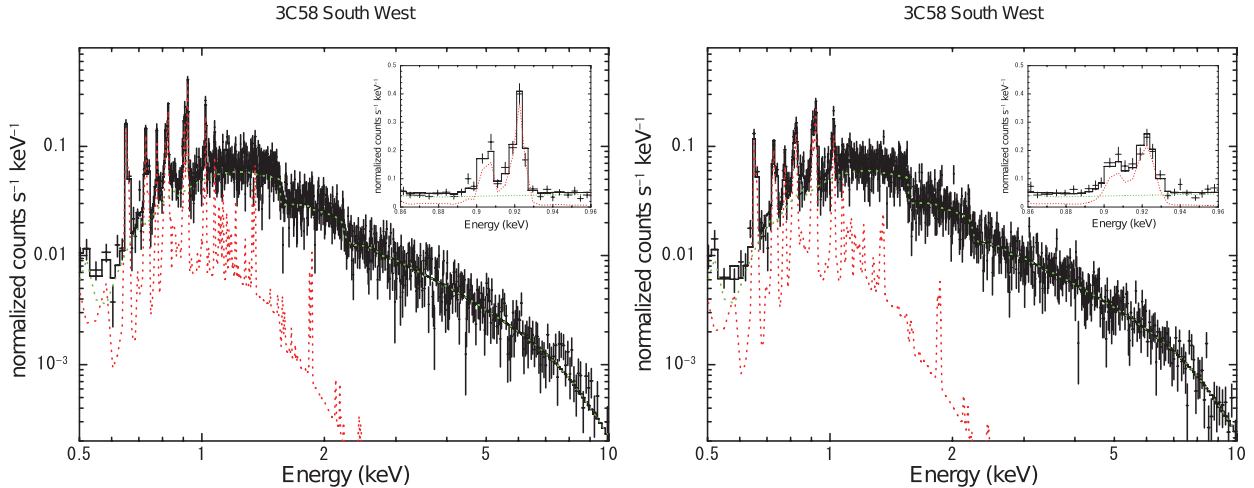


Figure 15: SXS simulation in the ISM case (left) and the ejecta case (right). Insets show an expanded view of Ne lines.

be SN 1181), the reverse shock velocity in the frame of the ejecta is likely to be expanding with a velocity of $3,000\text{--}4,000\text{ km s}^{-1}$. Combined with almost pure metal composition in the ejecta case, ion temperatures are still quite high likely to be several hundreds keV allowing us to measure the line broadening (see also Section 1.3.5).

G21.5–0.9: This PWN is a prototype example of a plerionic Composite-type SNR, originally thought to be a pure plerion like the Crab. Its age has been estimated as 870_{-150}^{+200} yr (Bietenholz & Bartel, 2008) based on the measured expansion speed of the radio nebula, while the pulsar’s characteristic age is 4.8 kyr (Gupta et al., 2005; Camilo et al., 2006). This PWN has been used as a calibration target for *Chandra*. With a flux of a few mCrab in X-rays, it’s not too bright to cause pile-up (like the Crab), while also bright enough to serve as a “standard” candle. It has been also used as a cross-calibration study for the instruments onboard currently active observatories: *Chandra*’s ACIS, *Suzaku*’s XIS, *Swift*’s XRT, and *XMM-Newton*’s EPIC (MOS and pn) for the soft X-ray band, and *INTEGRAL*’s IBIS-ISGRI, *RXTE*’s PCA, and *Suzaku*’s HXD-PIN for the hard X-ray band (Tsujimoto et al., 2011). Its size of $5'$ -diameter makes it is slightly larger than SXS’s field of view (FoV) but fits nicely within the HXI’s FoV.

The SXS’s unprecedented spectral resolution and sensitivity will help shed light on the nature of the thermal X-ray emission detected from the northern knots, allowing us to differentiate between a shocked ISM/CSM origin and a shock-heated ejecta origin, as hinted by the *Chandra* and *XMM-Newton* studies (Matheson & Safi-Harb, 2010; Bocchino et al., 2005). As well, the SXS will allow us to differentiate between a non-thermal or thermal spectrum for the eastern limb, which was not possible with the *XMM-Newton* and deep *Chandra* observations. In addition the HXI and SGD will extend the spectrum of the PWN up to as high as 300 keV, allowing for the first time to perform a broadband and sensitive spectral study that may reveal a spectral break or at least constrain the power-law photon index across orders of magnitude in energy.

The right panel of Figure 16 shows the *sim-x* simulated spectrum of the thermal X-ray emission detected from the knots north of the pulsar/PWN, acquired with a deep 500 ks SXS simulation pointing $\sim 2'.4$ north of the pulsar (to minimize contamination by the central PWN while maximizing the thermal emission from the knots). The dotted line illustrates the thermal component (*vpshock* model with a low ionization timescale of $2 \times 10^{10}\text{ cm}^{-3}\text{ s}$ and a high temperature of $\sim 5\text{ keV}$ mimicking the *Chandra* spectrum) associated with the knots. Other models were proposed for the emission from this region, including a two-component thermal spectrum with a much lower temperature ($kT \sim 0.2\text{ keV}$) plus a non-thermal hard component. Furthermore, while the *Chandra* data favour solar abundances (except for S), the *XMM-Newton* data did not rule out enhanced

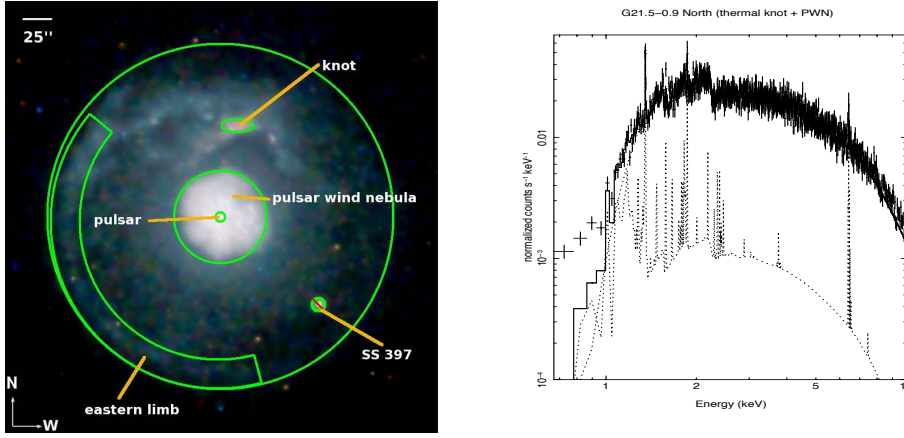


Figure 16: (Left) The *Chandra* image of G21.5–0.9 showing the bright central PWN with strong candidate regions for thermal X-ray emission: the northern knots which likely represent supernova ejecta, and the eastern limb showing the long-sought SNR shell (Matheson & Safi-Harb, 2010). (Right) A simulated deep (500 ks) SXS spectrum of the thermal emission from the northern knots for a pointing $\sim 2'.4$ north of the pulsar centred near the bright ‘knot’ shown to the left. The spectrum was simulated with *simx* using a thermal model (*vpshock*) based on the *Chandra* data.

abundances from Mg and Si.

Given the contamination by the central PWN in the SXS pointing at the knot, an additional non-thermal component was accounted for and was characterized by a power-law model with a photon index of 1.8. The line emission shown in Figure 16 shows the thermal contribution underneath dominant non-thermal PWN emission. The SXS pointing and exposure time were chosen such as the lines from the ejecta component will become visible and allow us to constrain the abundance ratios for Mg, Si, S and Fe, which was not possible with the CCD spectra. In particular an Fe-K line becomes clearly visible in the thermal interpretation with a hot temperature and for deep exposures (~ 500 ks). Furthermore, as mentioned above for 3C 58, it’s likely that the ion temperature is very high and that the Fe-K line is broadened under the assumption of a similarly young (≤ 1 kyr) SNR.

Similarly, a deep exposure of the eastern limb will help distinguish between a power-law and a thermal model (both were acceptable with the *Chandra* data of the eastern limb), and constrain (if thermal in nature) the abundance ratios and the ionization timescale which is needed to infer the conditions of the ambient medium in which G21.5–0.9 is expanding.

In Fig. 17, we show the simulated hard X-ray spectrum of G21.5–0.9 with the HXI (5–50 keV) and SGD (40–300 keV). To simulate the spectrum, we investigated the *Suzaku* data which were adequately fitted with a power-law model in the hard band, as found by Tsujimoto et al. (2011). However we also find that a broken power-law with a spectral break within the HXI band can not be ruled out. Using the XIS and PIN data, the broken power-law model has the following parameters: $\Gamma_1=1.9$ (XIS fit), $\Gamma_2=2.3$ (HXD-PIN fit) with a spectral break around 35 keV (although poorly constrained). Simulating the HXI and SGD data with this broken power-law model, a ≥ 200 ks exposure will allow us to distinguish between the broken power-law and the power-law models. Clearly, the energy coverage will extend beyond *NuSTAR*’s hard X-ray band, favouring *ASTRO-H* over *NuSTAR* for studying spectral breaks in PWNe.

We acknowledge contributions of B. Guest and H. Matheson (University of Manitoba) towards the simulations shown in Figures 16 and 17.

3.4 Beyond Feasibility

Thanks to SXS’s sensitivity, *ASTRO-H* will potentially open a new window to search for soft thermal X-ray emission that hasn’t been detected before and that may be associated with cold, un-shocked ejecta. Furthermore, deep X-ray observations of the more evolved PWNe, targeting the PWN regions crushed by the SNR’s reverse shock and observed in the TeV gamma-ray band, will address the evolution of PWNe and the nature of their

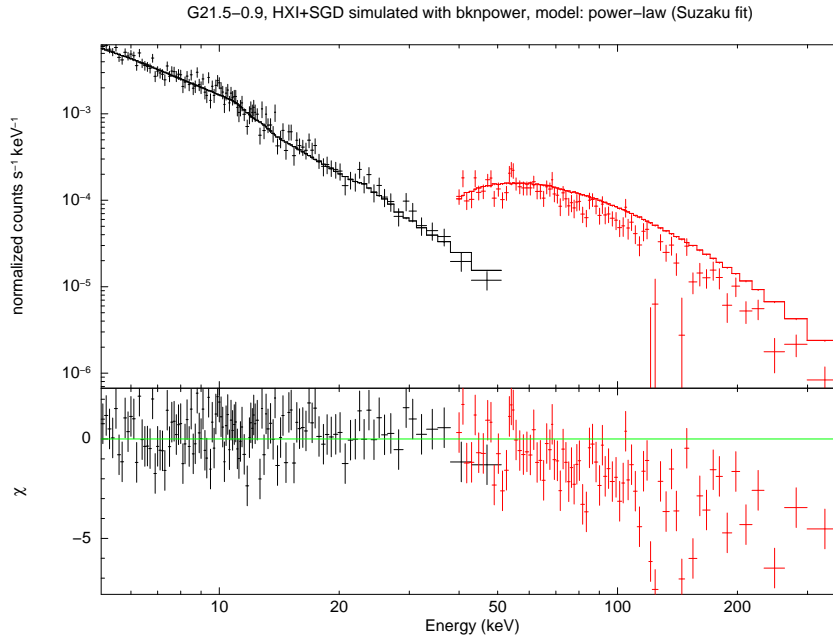


Figure 17: A 200 ks HXI (black) and SGD (red) simulated spectrum of the non-thermal, central, PWN based on the *Suzaku* data fitted with a broken power-law model. The model shown is an absorbed power-law model that provides an adequate fit to *Suzaku* data (Tsujiimoto et al., 2011). We note that here only the *nxb* background has been subtracted.

emission from keV to TeV energies. Finally, polarization studies with HXI and SGD of the brightest PWNe will potentially offer an innovative way to study their magnetic field driving their dominant non-thermal emission.

4 Conclusions for Old SNRs and Pulsar Wind Nebulae

Old SNRs are bright, soft X-ray sources that will have rich spectra dominated by lines in the case of limb-brightened and mixed-morphology remnants, and continuum emission in the case of the pulsar-wind nebulae. They are astrophysical laboratories for understanding the physics of shocks on the one hand, and for understanding the astrophysical nature of the ISM and SNRs on the other. We have highlighted a few of the more important types of observations of the more obvious targets that we expect will be carried out with *ASTRO-H*.

References

- Aharonian, F. et al. 2006, *A&A*, 448, L19
- Aschenbach, B., & Leahy, D. A. 1999, *A&A*, 341, 602
- Bamba, A., Koyama, K., & Tomida, H. 2000, *PASJ*, 52, 1157
- Bamba, A., Yamazaki, R., Yoshida, T., Terasawa, T., & Koyama, K. 2005, *ApJ*, 621, 793
- Bietenholz, M. & Bartel, N. 2008, *MNRAS*, 386, 1411
- Blair, W. P. et al., 2005, *AJ*, 129, 2268.
- Blondin, J.M., Chevalier, R.A., & Frierson, D.M. 2001, *ApJ*, 563, 806
- Bocchino, F., van der Swaluw, E., Chevalier, R., & Bandiera, R. 2005, *A&A*, 442, 539
- Bocchino, F. et al. 2010, *A&A*, 520, 71
- Bock, D.C.-J., Turtle, A.J., & Green, 1998, *AJ*, 116, 1886
- Bodewits, et al. 2007, *A&A*, 469, 1183
- Camilo, F., Ransom, S. M., Gaensler, B. M. et al. 2006, *ApJ*, 637, 456
- Cunha, K., Hubeny, I., & Lanz, T. 2006, *ApJ*, 647L, 143
- Danforth, C.W., Blair, W.P., & Raymond, J.C. 2001, *ApJ*, 122, 938
- Drake, J.J., & Testa, P. 2005, *Nature*, 436, 525
- Ferrand, G. & Safi-Harb, S. 2012, *Adv. Sp. Res.*, 49, 1313
- Gaensler, B. M., & Slane, P. O. 2006, *ARAA*, 44, 17
- Ghavamian, P., Laming, J.M., & Rakowski, C.E. 2007, *ApJ*, 654, L69
- Gotthelf, E. V., Helfand, D. J., & Newburgh, L. 2007, *ApJ*, 654, 267
- Green, D. A. 2009, *Bulletin of the Astronomical Society of India*, 37, 45
- Gupta, Y., Mitra, D., Green, D. A., & Acharyya, A. 2005, *Curr. Sci.*, 89, 853
- Hester, J. J. 2008, *ARAA*, 46, 127
- Hughes, J. P., Rakowski, C. E., & Decourchelle, A. 2000, *ApJL*, 543, L61
- Hwang, U., Petre, R., & Flanagan, K.A. 2008, *ApJ*, 676, 378
- Itoh, H., & Masai, K. 1989, *MNRAS*, 236, 885
- Iwamoto, K., Brachwitz, F., Nomoto, K., Kishimoto, N., Umeda, H., Hix, W. R., & Thielemann, F.-K. 1999, *ApJS*, 125, 439
- Kaasra, J.S., Bykov, A.M., & Werner, N. 2009, *A&A*, 503, 373
- Kargaltsev, O. & Pavlov, G. G. 2008, *American Institute of Physics Conference Series*, 983, 171
- Kargaltsev, O. & Pavlov, G. G. 2010, *American Institute of Physics Conference Series*, 1248, 25
- Katsuda, S., & Tsunemi, H. 2005, *PASJ*, 57, 621
- Katsuda, S., & Tsunemi, H. 2006, *ApJ*, 642, 917
- Katsuda, S., Tsunemi, H., Uchida, H., Miyata, E., Nemes, N., Miller, E.D., Mori, K., Hughes, J.P. 2008, *PASJ*, 60, S115
- Katsuda, S., Mori, K., Petre, R., et al. 2011, *PASJ*, 63, 827
- Katsuda, S., et al., 2011, *ApJ*, 730, 24
- Kawasaki, M. T., Ozaki, M., Nagase, F., Masai, K., Ishida, M., & Petre, R. 2002, *ApJ*, 572, 897
- Klein, R.I., Budil, K.S., Perry, T.S., & Bach, D.R. 2003, *ApJ*, 583, 245
- Koyama, K., Petre, R., Gotthelf, E. V., et al. 1995, *Nature*, 378, 255
- Ku, W. H.-M., Kahn, S. M., Pisarski, R., & Long, K. S. 1984, *ApJ*, 278, 615
- LaMassa, S.M., Slane, P.O., & de Jager, O.C. 2008, *ApJ*, 689, 121
- Lazendic, J. S., & Slane, P. O. 2006, *ApJ*, 647, 350
- Levenson, N. A., Graham, J. R., Achenbach, B., et al. 1997, *ApJ*, 484, 304
- Levenson, N. A., Graham, J. R., Keller, L. D., & Richter, M. J. 1998, *ApJS*, 118, 541
- Lu, F.J., & Aschenbach, B. 2000, *A&A*, 362, 1083
- Matheson, H. & Safi-Harb, S. 2005, *ASR*, 35, 1099
- Matheson, H. & Safi-Harb, S. 2010, *ApJ*, 724, 572
- McCray, R., & Snow, T. P., Jr. 1979, *ARAA*, 17, 213
- McEntaffer, R.L., & Brantseg, T. 2011, *ApJ*, 730, article id.99
- Masai, K., Dogiel, V.A., Inoue, H., Schoifelder, V., & Strong, A.W. 2002, *ApJ*, 581, 1071
- Miceli, M., Reale, F., Orlando, S., & Bocchino, F. 2006, *A&A*, 458, 213
- Miceli, M., Bocchino, F., & Reale, F. 2008, *ApJ*, 676, 1064
- Miceli, M., Bocchino, F., Maggio, A., & Reale, F. 2005, *A&A*, 442, 513
- Mitsuda, K., et al. 2010, *Prof. of SPIE*, 7732, 29
- Miyata, E., et al., 1994, *PASJ*, 46, 101
- Miyata, E., et al., 1998, *PASJ*, 50, 257
- Miyata, E., Masai, K., & Hughes, J.P. 2008, *PASJ*, 60, 521
- Miyata, E., & Tsunemi, H. 2001, *ApJ*, 552, 624
- Miyata, E., Tsunemi, H., Aschenbach, B., & Mori, K. 2001, *ApJ*, 559, L45

- Nakamura, R., Bamba, A., Ishida, M., et al. 2014, PASJ, 66, 62
- Ozawa, M., Koyama, K., Yamaguchi, H., Masai, K., & Tamagawa, T. 2009, ApJ, 706, L71
- Pavlov, G. G., Teter, M. A., Kargaltsev, O., & Sanwal, D. 2003, ApJ, 591, 1157
- Pittard, J.M., Hartquist, T.W., & Falle, S.A.E.G. 2010, MNRAS, 405, 821
- Preite Martinez, A. 2011, A&A, 527, A55
- Reynolds, S. P. 2009, ApJ, 703, 662
- Rho, J., & Petre, R. 1998, ApJ, 503, L167
- Safi-Harb, S. 2012, American Institute of Physics Conference Series, 1505, 13 (arXiv:1210.5406)
- Safi-Harb, S. 2013, Proceedings of the International Astronomical Union, 291, 251 (arXiv:1211.0852)
- Safi-Harb, S., Harrus, I. M., Petre, R., Pavlov, G. G., Koptsevich, A. B., & Sanwal, D. 2001, ApJ, 561, 308
- Sawada, M., & Koyama, K. 2012, PASJ, 64, 81
- Seward, F. D., Gorenstein, P., & Smith, R. K. 2006, ApJ, 636, 873
- Shelton, R. L., Cox, D. P., Maciejewski, W., Smith, R. K., Plewa, T., Pawl, A., & Różycka, M. 1999, ApJ, 524, 192
- Shelton, R. L., Kuntz, K. D., & Petre, R. 2004, ApJ, 615, 275
- Shimizu, T., Masai, K., & Koyama, K. 2012, PASJ, 64, 24
- Slane, P. 2008, American Institute of Physics Conference Series, 1085, 120
- Slane, P. O., Helfand, D. J., Van der Swaluw, E., & Murray, S. S. 2004, ApJ, 616, 403
- Slane, P., Chen, Y., Schulz, N. S., Seward, F. D., Hughes, J. P., Gaensler, B. M. 2000, ApJ, 533, L29
- Tsujimoto, M., Guainazzi, M., Plucinsky, P. P., Beardmore, A. P., Ishida, M., Natalucci, L., Posson-Brown, J. L. L., Read, A. M., Saxton, R. D., & Shaposhnikov, N. V. 2011, A&A, 525, 25
- Tsunemi, H., et al., 2007, ApJ, **671**, 1717
- Tsunemi, H., et al. 2010, Proc. of SPIE, 7732, 28
- Tsunemi, H., Miyata, E., & Aschenbach, B. 1999, PASJ, 51, 711
- Uchida, H., Tsunemi, H., Katsuda, S., Kimura, M., Kosugi, H., Takahashi, H. 2009, PASJ, 61, 503
- Uchida, H., et al., 2011, PASJ, **63**, 199
- Uchida, H., et al., 2009c, ApJ, **705**, 1152
- Uchida, H., Koyama K., Yamaguchi, H., et al. 2012, PASJ, **64**, 141
- Vink, J. 2012, A&A Rev., 20, 49
- Vink, J., Kaastra, J.S., & Bleeker, J.A.M. 1997, 328, 628
- White, R. L., & Long, K. S. 1991, ApJ, 373, 543
- Wilms, J., Allen, A., & McCray, R. 2000, ApJ, 542, 914
- Woosley, S. E., & Weaver, T. A. 1995, ApJS, 101, 181
- Yamaguchi, H., Koyama, K., Nakajima, H., Bamba, A., Yamazaki, R., Vink, J., & Kawachi, A. 2008, PASJ, 60, S123
- Yamaguchi, H., Ozawa, M., Koyama, K., Masai, K., Hiraga, J. S., Ozaki, M., & Yonetoku, D. 2009, ApJ, 705, L6
- Yamaguchi, H., Ozawa, M., & Ohnishi, T. 2012, Advances in Space Research, 49, 451
- Yusef-Zadeh, F., Wardle, M., Rho, J., & Sakano, M. 2003, ApJ, 585, 319
- Zhou, X., Bocchino, F., Miceli, M., Orlando, S., & Chen, Y. 2010, MNRAS, 406, 223